DEPARTMENT OF PHYSICS
UNIVERSITY OF JYVÄSKYLÄ
RESEARCH REPORT No. 6/2017

Spectroscopy and lifetime measurements of ^{166,168}Os

by

Sanna Stolze

Academic Dissertation
for the Degree of
Doctor of Philosophy

To be presented, by permission of the
Faculty of Mathematics and Science
of the University of Jyväskylä,
for public examination in Auditorium FYS1 of the
University of Jyväskylä on October 27, 2017
at 12 o'clock noon

Jyväskylä, Finland
October 2017

Abstract

Stolze, Sanna
Spectroscopy and lifetime measurements of ^{166,168}Os
Jyväskylä: University of Jyväskylä, 2017, 76 p.
Department of Physics Research Report No. 6/2017
ISSN: 1234-465X; 6/2017
ISBN: 978-951-39-7207-3 (paper version)
ISBN: 978-951-39-7208-0 (electronic version)
Diss.

Neutron-deficient osmium isotopes ^{166}Os and ^{168}Os have been studied with γ-ray spectroscopy and lifetime measurements. The level scheme of ^{166}Os has been expanded with several new structures including second the 8^+ and 10^+ states. These states confirm the change in the structure of the yrast band between the 6^+ and 8^+ states. Lifetimes of the low-lying excited states have been measured in an RDDS measurement. The results reveal a sudden decrease in the collectivity when moving towards the neutron shell closure. While the $2^+ \rightarrow 0^+$ transition is still collective in ^{168}Os, in ^{166}Os the reduced transition probability is only few Weisskopf units, a value expected only at closed shells. In ^{168}Os the $4^+ \rightarrow 2^+$ transition is remarkably less collective than the $2^+ \rightarrow 0^+$ transition. While nuclear models predict a decrease in collectivity, no modern calculations can explain the measured transition probabilities.

Keywords: nuclear structure, nuclear spectroscopy, γ-ray spectroscopy, lifetime measurements, reduced transition probabilities

Author's address Sanna Stolze
Department of Physics
University of Jyväskylä
Finland

Supervisors Dr. Tuomas Grahn
Department of Physics
University of Jyväskylä
Finland

Prof. Rauno Julin
Department of Physics
University of Jyväskylä
Finland

Reviewers Dr. Gregory Lane
Department of Nuclear Physics
Australian National University
Canberra
Australia

Dr. Joa Ljungvall
CSNSM - UMR8609
Orsay
France

Opponent Dr. Marcus Scheck
University of the West of Scotland
Paisley
Scotland
United Kingdom

Preface

The work has been carried out during the years 2010-2017 at the Department of Physics of the University of Jyväskylä.

I would like to thank my supervisors Dr. Tuomas Grahn and Prof. Rauno Julin for the guidance and support during these years. You have tried to keep me on the track of concentrating on the relevant topics for the thesis, a task that has not been easy. I want to thank also Dr. Catherine Scholey, Dr. Sakari Juutinen and Dr. David Joss for the help with the level scheme of ^{166}Os, as it would have never been completed without your help.

These years would have been different without the whole RITU-Gamma group. A special thanks goes to Dr. Pauli Peura and Dr. Ulrika Jakobsson for teaching us how things work in the lab and Mr. Joonas Konki, Mr. Jari Partanen and Mr. Hussam Badran for the countless hours spent in the detector hospital and the RITU cave setting up the germanium detectors for the experiments.

Coffee breaks and other breaks would have been different without the company of friends. Thank you all.

In the end I want to thank my mother, father, sister and brother for all of the support. And last, but not the least, Kalle. Thank you for everything.

Sanna Stolze
Jyväskylä, October, 2017

List of Publications

The thesis is based on the work of ^{166}Os and ^{168}Os. For ^{168}Os the results have been published in publication 1. The author has contributed to the experimental part of publications 2-36.

1. *Excited states and reduced transition probabilities in ^{168}Os*
   T. Grahn, S. Stolze *et al.*.
   Phys. Rev. C **94**, no. 4, 044327 (2016).

2. *Reduced transition probabilities along the yrast line in ^{166}W*
   B. Saygi *et al.*.
   Phys. Rev. C **96**, no. 2, 021301 (2017).

3. *Detailed spectroscopy of ^{195}Bi*
   A. Herzan *et al.*.
   Phys. Rev. C **96**, no. 1, 014301 (2017).

4. *De-excitation of the strongly coupled band in ^{177}Au and implications for core intruder configurations in the light Hg isotopes*
   M. Venhart *et al.*.
   Phys. Rev. C **95**, no. 6, 061302 (2017).

5. *Lifetime measurements of excited states in ^{162}W and ^{164}W and the evolution of collectivity in rare-earth nuclei*
   M. Doncel *et al.*.
   Phys. Rev. C **95**, no. 4, 044321 (2017).

6. *Experimental study of isomeric intruder 12^+ states in $^{187,203}At$*
   K. Auranen *et al.*.
   Phys. Rev. C **95**, no. 4, 044311 (2017).

7. *Backbending in the pear-shaped $^{223}_{90}Th$ nucleus: Evidence of a high-spin octupole to quadrupole shape transition in the actinides*
   G. Maquart *et al.*.
   Phys. Rev. C **95**, no. 3, 034304 (2017).

8. *In-beam study of ^{253}No using the SAGE spectrometer*
   A. K. Mistry *et al.*.
   Eur. Phys. J. A **53**, no. 2, 24 (2017).

9. *Towards saturation of the electron-capture delayed fission probability: The new isotopes ^{240}Es and ^{236}Bk*
   J. Konki *et al.*.
   Phys. Lett. B **764**, 265 (2017).

10. *Collective 2^{+1} excitations in ^{206}Po and $^{208,210}Rn$*
    T. Grahn *et al.*.
    Eur. Phys. J. A **52**, no. 11, 340 (2016).

11. *Spectroscopy of ^{70}Kr and isospin symmetry in the $T = 1fpg$ shell nuclei*
    D. M. Debenham *et al.*.
    Phys. Rev. C **94**, no. 5, 054311 (2016).

12. *Confirmation of the new isotope ^{178}Pb*
    H. Badran *et al.*.
    Phys. Rev. C **94**, no. 5, 054301 (2016).

13. *Deformation of the proton emitter ^{113}Cs from electromagnetic transition and proton-emission rates*
    D. Hodge *et al.*.
    Phys. Rev. C **94**, no. 3, 034321 (2016).

14. *Direct observation of the $^{114}Ba \rightarrow ^{110}Xe \rightarrow ^{106}Te \rightarrow ^{102}Sn$ triple α-decay chain using position and time correlations*
    L. Capponi *et al.*.
    Phys. Rev. C **94**, no. 2, 024314 (2016).

15. *Identification of the $J\pi$=1- state in ^{218}Ra populated via α decay of ^{222}Th*
    E. Parr *et al.*.
    Phys. Rev. C **94**, no. 1, 014307 (2016).

16. *Lifetime measurements in ^{166}Re : Collective versus magnetic rotation*
H. J. Li *et al.*.
Phys. Rev. C **93**, no. 3, 034309 (2016).

17. *Excited states in the proton-unbound nuclide ^{158}Ta*
R. J. Carroll *et al.*.
Phys. Rev. C **93**, no. 3, 034307 (2016).

18. *Identification of a dipole band above the $I\pi = 31/2^-$ isomeric state in ^{189}Pb*
D. Hodge *et al.*.
Phys. Rev. C **92**, no. 5, 054312 (2015).

19. *Spectroscopy of low-lying states in neutron-deficient astatine and francium nuclei*
U. Jakobsson *et al.*.
AIP Conf. Proc. **1681**, 030014 (2015).

20. *Decay and Fission Hindrance of Two- and Four-Quasiparticle K Isomers in ^{254}Rf*
H. M. David *et al.*. PhysRevLett.115.132502
Phys. Rev. Lett. **115**, no. 13, 132502 (2015), Addendum: [Phys. Rev. Lett. *115*, no. 16, 169902 (2015)].

21. *Recoil-decay tagging spectroscopy of $^{162}_{74}W_{88}$*
H. J. Li *et al.*.
Phys. Rev. C *92*, no. 1, 014326 (2015).

22. *First identification of rotational band structures in $^{166}_{91}Re_{75}$*
H. J. Li *et al.*.
Phys. Rev. C *92*, no. 1, 014310 (2015).

23. *Lifetime measurement of the first excited 2^+ state in ^{112}Te*
M. Doncel *et al.*.
Phys. Rev. C *91*, no. 6, 061304 (2015).

24. *Oblately deformed isomeric proton-emitting state in ^{151}Lu*
M. J. Taylor *et al.*.
Phys. Rev. C **91**, no. 4, 044322 (2015).

25. *Spectroscopy of ^{201}At including the observation of a shears band and the $29/2^+$ isomeric state*
K. Auranen *et al.*.
Phys. Rev. C **91**, no. 2, 024324 (2015), Erratum: [Phys. Rev. C *92*, no. 3, 039901 (2015)].

26. *Spectroscopy of ^{161}Hf from low to high spin*
P. J. R. Mason *et al.*.
Phys. Rev. C **90**, no. 5, 054331 (2014).

27. *Spectroscopy on the proton drip-line: Probing the structure dependence of isospin nonconserving interactions*
J. Henderson *et al.*.
Phys. Rev. C **90**, no. 5, 051303 (2014).

28. *Experimental study of 12^+ isomers in $^{199,201}At$*
K. Auranen *et al.*.
Phys. Rev. C **90**, no. 2, 024310 (2014).

29. *Competing single-particle and collective states in the low-energy structure of ^{113}I*
M. J. Taylor *et al.*.
Phys. Rev. C **88**, no. 5, 054307 (2013).

30. *Proton emission from an oblate nucleus ^{151}Lu*
M. G. Procter *et al.*.
Phys. Lett. B **725**, 79 (2013).

31. *Spectroscopy of proton-rich ^{66}Se up to $J^\pi = 6^+$: Isospin-breaking effect in the $A = 66$ isobaric triplet*
P. Ruotsalainen *et al.*.
Phys. Rev. C **88**, no. 4, 041308 (2013)

32. *Enhancing the sensitivity of recoil-beta tagging*
J. Henderson *et al.*.
JINST **8**, P04025 (2013).

33. *High-precision mass measurements of $^{203-207}Rn$ and ^{213}Ra with SHIPTRAP*
C. Droese *et al.*.
Eur. Phys. J. A **49**, 13 (2013).

34. *Isomer-tagged differential-plunger measurements in* $^{113}_{54}Xe$
M. G. Procter *et al.*.
Phys. Rev. C **87**, no. 1, 014308 (2013).

35. *Identification of isomeric states in the* $N = 73$ *neutron-deficient nuclei* ^{132}Pr *and* ^{130}La
M. J. Taylor *et al.*.
Phys. Rev. C **86**, 044310 (2012).

36. *High-K four-quasiparticle states in* ^{138}Gd
M. G. Procter *et al.*.
Phys. Rev. C **83**, 034311 (2011).

Contents

Chapter 1

Introduction

One way of characterizing a nucleus is the number of protons and neutrons that form the nucleus. The atomic number Z is the number of protons in the nucleus. It identifies the element in question and determines the number of electrons in the atom and therefore its chemical properties. The nuclei studied in this work have $Z = 76$ and are osmium isotopes. They have different neutron number N, ^{166}Os has $N = 90$ and ^{168}Os has $N = 92$. The mass number A is the sum of protons and neutrons $A = Z + N$, which are collectively known as nucleons. Both types of the nucleons consist of three quarks, which are elementary particles. The quarks are bound inside the nucleon with the strong force. The quarks are fermions and can not have the same quantum numbers. Also, the nucleons formed by three quarks are fermions and have to obey the Pauli principle.

There are approximately 300 different nuclei that occur naturally on Earth. Most of these are stable, but a few are radioactive and decay, like ^{235}U which decays by α decay or fission and ^{14}C which β decays. Besides these nuclei found in nature, around 2000 more have been produced in laboratories around the world. These nuclei are normally short lived and decay in times of nanoseconds to hours. Theories predict approximately 8000 bound nuclei to exist before the excess of protons or neutrons is too large [Erler12].

The structure of nuclei can be studied with γ-ray spectroscopy, which is a

sensitive and versatile tool especially when combined with ancillary detectors. For instance, sudden changes in energies of the first excited states indicate the evolution of shell structures when moving away from the valley of stability. More precise information about the underlying structures can be obtained by measuring the reduced transition probabilities with Coulomb excitation [Alder75, Görgen10] or lifetime measurements of excited states, described in this thesis.

The measured Coulomb-excitation cross sections of lifetimes of excited states can be used to deduce the corresponding reduced transition probabilities. Low reduced transition probabilities mean that the transitions are created by an excitation or de-excitation of a single proton or neutron. These type of transitions are common for nuclei near the closed shells. High reduced transition probabilities correspond to collective excitations and deformed nuclear shapes. These are observed for the lowest excited states at mid-shell, where the number of protons and neutrons participating to the excitations is the highest [Bohr98][Krane88]. A more detailed study of the reduced transition probabilities can reveal interesting and unexpected phenomena. For example, the region around doubly-magic ^{100}Sn has been under investigation for enhanced transition probabilities when approaching the $N = 50$ shell-closure [Guastalla13, Ekström08, Banu05, Cederkäll07]. Also in the lead isotopes the reduced transition probabilities from the first 2^+ states are smaller at the neutron mid-shell than at intermediate mass numbers $A = 196, 198$ [Pakarinen17].

Near the closed shell the transition probabilities of the $2^+ \rightarrow 0^+$ transitions in even-even nuclei are not enough to determine the collectivity of the structures at higher spin due to mixing of different structures (i.e. shape coexistence, see [Heyde83, Wood92, Heyde11]), as can be seen in mercury isotopes [Grahn09, Bree14a]. Instead reduced transition probabilities have to be measured also for higher-lying states, which are usually less mixed. Shape coexistence is expected to disappear when moving away from the closed shell to more deformed structures.

The region of the nuclear chart around the $N = 104$ neutron mid-shell below the $Z = 82$ shell closure has been investigated intensively, (see, for example reviews by Julin [Julin16]) . The increase of α-decay branching ratio when moving towards the more neutron-deficient nuclei enables prompt spectroscopy with

low production cross-sections with recoil-decay tagging (see section 3.5). At the neutron mid-shell the excited states are highly collective with low and almost identical energiesfor the 2^+ states for even-even isotopes. With decreasing neutron number the prolate structures evolve to shape coexistence and finally to vibrational structures when approaching the closed neutron shell.

For osmium nuclei, excited states have been studied from ^{162}Os [Joss04] to ^{198}Os [Podolyák09], covering almost all of the known osmium isotopes. In ^{162}Os the observed energy spacings of the first excited states indicate vibrational structures. Shape coexistence has been observed in ^{172}Os [Davidson94]. At the neutron mid-shell the states are collective and the nuclei appear to have prolate deformation. A similar, though reversed, trend can be observed for increasing neutron number. At $N = 120$ the energies of the first excited states indicate vibrational structures again [John14, Podolyák09].

In the present work, ^{166}Os and ^{168}Os have been studied. The excited states of ^{166}Os have been investigated with γ-ray spectroscopy enabled by recoil-decay tagging with the characteristic α decay. Also the lifetimes of the first excited states in both isotopes have been measured with the Recoil Distance Doppler-Shift technique. This makes ^{166}Os the most neutron-deficient nucleus in which lifetime measurements have been carried out when looking at the number of neutrons removed from the stable isotopes. The newly obtained properties will be used to probe the shape evolution in these exotic, neutron-deficient nuclei.

Chapter 2

Theoretical background

2.1 Radioactivity

Out of the 3000 known nuclei only approximately 280 are stable. The rest decay into other nuclei via alpha, beta, neutron or proton decay or by fission. The decays can be characterized by the energy released in the decay and the mean lifetime of the decaying nucleus.

All of the decays follow the exponential decay law,

$$n(t) = n_0 e^{-\lambda t}, \tag{2.1}$$

where $n(t)$ is the number of nuclei at the time t and n_0 is the initial number of the nuclei. The decay is characterized by the decay constant λ which is unique to every decay and is related to the mean lifetime τ of the nucleus, or half-life $t_{1/2}$ that describes the time in which half of the nuclei have decayed, by

$$\lambda = \frac{1}{\tau} = \frac{\ln 2}{t_{1/2}}. \tag{2.2}$$

If there are several different decay modes, the corresponding decay constants

can be added together to form the total decay constant

$$\lambda_{\text{tot}} = \sum_i \lambda_i. \tag{2.3}$$

Besides the radioactive decay (α, β decay, proton or neutron emission or fission) of the nuclei, also the excited states of nuclei show such characteristic lifetimes with every state having a (different) lifetime.

For a more complicated system such as the excited states of a nucleus, equation 2.1 can be expanded to a set of equations, first introduced by Bateman. With levels L_i feeding level L_j, the time behavior of level L_j can be written as

$$\frac{\mathrm{d}}{\mathrm{d}t} n_j(t) = -\lambda_j n_j(t) + \sum_{i<j}^{N} \lambda_i n_i(t) b_{ji}, \tag{2.4}$$

where b_{ji} is the branching ratio for the transition $L_i \rightarrow L_j$. Only N feeding levels are taken into account. When some of the levels L_i have another set of levels feeding them, the situation gets more complicated and will be discussed later.

2.2 Gamma-ray transitions and reduced transition probabilities

Excited states in a nucleus normally de-excite via electromagnetic transitions, either by emission of a γ ray or by internal conversion [Krane88]. Charged-paticle decay or fission directly from an isomeric state is possible, if the lifetime of the state is long enough. For example, the 19^- state in ^{158}Ta has a half-life of 6.1(1) µs and has an α-decay branch [Carroll14].

The electromagnetic transitions are of either electric or magnetic type. The multipole order of the transition is 2^L, where L is the quantum number, often called multipolarity, associated to the angular momentum transferred in the transition. Conservation of angular momentum and parity sets selection rules for

the angular momentum and the type of the transition. The angular momentum $\mathbf{L}$ is constricted by $\mathbf{J}_i + \mathbf{L} + \mathbf{J}_f = 0$, where $\mathbf{J}_i$ and $\mathbf{J}_f$ are the angular momenta of the initial and final state.They are also called nuclear spins or just spins, not to be confused with the quantum mechanical spin $\mathbf{S}$, as they are already the sum of the orbital angular momenta $\mathbf{L}$ and spin, $\mathbf{J} = \mathbf{L} + \mathbf{S}$. This gives $|J_i - J_f| < L < |J_i + J_f|$ for the corresponding quantum numbers. No $L = 0$ transitions are possible via single γ-ray emission. With parities of the initial and final state $\pi_i\pi_f = +1$ only even L values are allowed for electric transitions (and odd for magnetic). For $\pi_i\pi_f = -1$ only odd values for L are possible in electric transition (and even for magnetic).

There are usually several different transition modes available, if the spins of the initial and final states are non-zero. The transition with the lowest multipole is normally the strongest. This can be seen from the Weisskopf estimates presented in table 2.1. Normally the lowest transition mode is several orders of magnitude stronger than the second lowest. The only exception to this are the $M1$ and $E2$ transitions, which can be strongly mixed.

In internal conversion an electron from the atom (or ion) is emitted. No γ ray is involved in the process. The rate of internal conversion is proportional to the transition matrix element similarly to the γ-ray transition. The electron states have an effect on the decay rate: for a fully stripped ion, internal conversion is not possible. Generally, internal conversion is more important for the high Z elements, higher multipolarities and low transition energies. A special case are the $0^+ \rightarrow 0^+$ transitions, which can not proceed via emission of a single γ ray. The conversion coefficient

$$\alpha = \frac{N_e}{N_\gamma} \tag{2.5}$$

describes the probability that the transition proceeds via internal conversion compared to the probability of γ-ray emission. Conversion coefficients can be calculated from atomic factors [Kibédi08].

The transition probability for γ-ray transitions can be written as [Suhonen07]

$$\lambda_{fi}^{(\sigma L)} = \frac{2}{\epsilon_0 \hbar} \frac{L+1}{L[(2L+1)!!]^2} \left(\frac{E_\gamma}{\hbar c}\right)^{2L+1} |\langle \xi_i J_i m_i | \mathcal{M}_{\sigma L \mu} | \xi_f J_f m_f \rangle|^2, \quad (2.6)$$

where σ is the type of the transition with E for the electric and M for magnetic the transition. L and μ are the quantum numbers for the angular momentum and its projection. E_γ is the transition energy and $\langle \xi_i J_i m_i | \mathcal{M}_{\sigma L \mu} | \xi_f J_f m_f \rangle$ is the nuclear matrix element of the transition $\langle \xi_i J_i m_i | \rightarrow \langle \xi_f J_f m_f |$. The rest of the quantum numbers for the states, besides the angular momentum and its projection, are denoted by ξ.

Because measurements are not sensitive to the magnetic substates, equation 2.6 is often rewritten as

$$\lambda_{fi}^{(\sigma L)} = \frac{2}{\epsilon_0 \hbar} \frac{L+1}{L[(2L+1)!!]^2} \left(\frac{E_\gamma}{\hbar c}\right)^{2L+1} B(\sigma L; \xi_i J_i \rightarrow \xi_f J_f), \quad (2.7)$$

where

$$B(\sigma L; \xi_i J_i \rightarrow \xi_f J_f) = \frac{1}{2J_i + 1} |\langle \xi_f J_f | |\mathcal{M}_{\sigma L}| | \xi_i J_i \rangle|^2 \quad (2.8)$$

is the reduced transition probability and $\langle \xi_f J_f | |\mathcal{M}_{\sigma L}| | \xi_i J_i \rangle$ the reduced transition matrix element.

The electric and magnetic operators can be written as

$$\mathcal{M}_E = \sum_{j=1}^{A} e(j) r_j^\lambda Y_{L\mu}(\Omega_j) \quad (2.9)$$

and

$$\mathcal{M}_M = \frac{\mu_N}{\hbar c} \sum_{j=1}^{A} \left[\frac{2}{L+1} g_l^{(j)} \mathbf{l}(j) + g_s^{(j)} \mathbf{s}(j) \right] \nabla_j [r_j^\lambda Y_{\lambda\mu}(\Omega_j)]. \quad (2.10)$$

Here $e(j)$ is the effective charge and $\mathbf{l}(j)$ and $\mathbf{s}(j)$ are the orbital angular

momentum and the spin, r_j^L and $Y_{L\mu}(\Omega_j)$ are the radial and spherical tensor operators, μ_N is the nuclear magneton, $\mu_N = \frac{e\hbar}{2m_p}$ and g_l and g_s are the g-factors. The effective charges $e(j)$ are used to replace the charges of proton and neutron in order to compensate in shell-model calculations for the restricted valence space [Suhonen07], see section 2.3.

It is clear from equations 2.7 and 2.8 that lifetime measurements give information about the wave functions of the initial and final states. As both of the operators in equations 2.9 and 2.10 are known, knowing the lifetimes of excited states enables testing of the wave functions.

For $E2$ transitions, the reduced transition probability in equation 2.7 can be written as

$$B(E2; J_i \to J_f) = \frac{0.0816}{\tau E_\gamma^5 (1+\alpha)} \tag{2.11}$$

by inserting the constants and rearranging. The transition probability is given in the units of $e^2\mathrm{b}^2$, γ-ray energy in MeV, lifetime in picoseconds and α is the conversion coefficient for the transition. In this only the $E2$ transition is taken into account. If there are other transition modes, their contribution to the lifetime has to be taken into account by multiplying the equation with $\lambda_{E2}/\lambda_{\mathrm{tot}}$.

2.3 Shell model

The nuclear shell model [Mayer48, Haxel49] provides a good descripion of spherical light to medium-heavy nuclei. It can explain and predict many nuclear properties such as the mean charged radii, neutron and proton separation energies and energies of excited states. The single-particle shell model, which is the simplest form of shell model [Krane88, Suhonen07], is presented here.

The nuclear shell model is similar to the atomic shell model, which explains the electron states in atoms. Instead of a nucleus creating an essentially well-defined Coulomb potential for all of the electrons, the nucleons feel the strong force of the other nucleons. This makes modeling the situation harder than for the

electrons, as perturbation theory does not work well for the strong force and the potential is created by nucleons themselves.

Due to the Pauli principle and the fact that protons and neutrons are fermions, two protons or neutrons can not occupy the same quantum states. This enables treating them as independent particles moving in a central potential created by the other nucleons. Besides the central potential, also a spin-orbit interaction $V_{so} \propto \mathbf{l} \cdot \mathbf{s}$ is needed to reproduce the spins and parities of odd-mass nuclei. A combination of the potential and the interaction generates gaps in level energies at certain nucleon numbers, which are known as magic numbers. The nuclei having either proton or neutron number magical are more strongly bound than the neighboring nuclei. An example of the energy levels is shown in figure 2.1. There are clear gaps in the level spacing at numbers 2, 8, 20, 28, 50, 82 and 126. The last gap has only been observed for neutrons so far. These numbers have been experimentally confirmed with binding energies and many other observables for nuclei near beta-stability. When moving to more exotic proton and neutron numbers, it is possible for these shell closures to evolve [Sorlin08].

In a simplified picture for an even-even nucleus, all the protons and neutrons couple into 0^+ pairs. For an odd nucleus the ground state is formed by filling the orbitals of figure 2.1 with up to $2j + 1$ protons and neutrons each. The last odd nucleon in the highest energy partially filled level determines the spin and parity of the ground state and the excited states can be formed by placing the nucleon on a higher-lying level. This is called a single-particle excitation. The lowest excitation energy is normally obtained by exciting the last nucleon to the next level, or by exciting a nucleon from a fully occupied orbital to the next available orbital and, therefore, creating a hole.

In reality, a simple potential is not enough to describe the interactions of a nucleus, but a residual interaction and further corrections [Tsunoda17] are needed. As these more complicated shell-model calculations require diagonalization of large matrices, the number of single-particle levels included has to be constrained. Near closed shells one can assume that only one main shell is included and thus the shell model performs well. It is also possible to calculate the shell model states for a deformed potential. This model meant for deformed nuclei is known as the Nilsson model [Nilsson55].

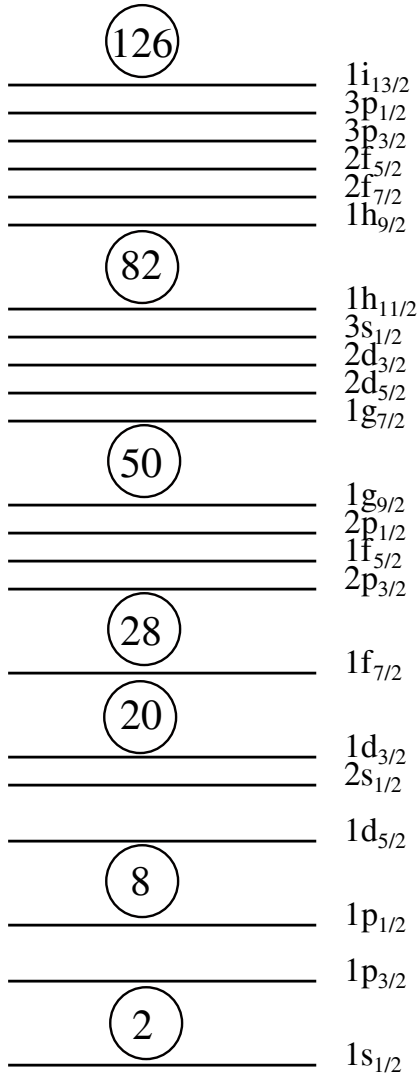

Figure 2.1. A schematic drawing of the single-particle energy levels in the shell model. Exact level positions depend on the potential and interaction that are used. The levels are labeled by the number of nodes in the wave function, the orbital angular momentum l and the total angular momentum j. For orbital angular momentum l the letters, $s = 0$, $p = 1$, $d = 2$, $f = 3$, $g = 4$, $h = 5$, $i = 6$ are used.

Table 2.1. Single-particle Weisskopf estimates for the decay constants and reduced transition probabilities for the lowest transition multipolarities. The transition energies are in MeV, decay constants in s^{-1} and the transition probabilities in e^2b^{2L} for electric transitions and in $(\mu_N/c)^2fm^{2L-2}$ for magnetic transitions.

EL	λ	$B(EL)$	ML	λ	$B(ML)$
$E1$	$1.0 \times 10^{14} A^{2/3} E^3$	$6.446 A^{2/3}$	$M1$	$5.6 \times 10^{13} E^5$	1.790
$E2$	$7.3 \times 10^7 A^{4/3} E^5$	$0.594 A^{4/3}$	$M2$	$3.5 \times 10^7 A^{2/3} E^5$	$1.650 A^{2/3}$
$E3$	$34 A^2 E^7$	$0.594 A^2$	$M3$	$16 A^{4/3} E^7$	$1.650 A^{4/3}$

The single-particle shell model can be used to find approximate reduced transition probabilities. These estimates are known as Weisskopf estimates or Weisskopf units (W.u). They can be calculated by taking a single-particle state with a wave function that is constant inside the nucleus and zero outside it. Integration of the equations 2.9 and 2.10 [Suhonen07] gives simple expressions for nuclei having the radius $R = R_0 A^{1/3}$, where R_0 is usually taken as 1.2 fm. These are listed in table 2.1 for the lowest multipolarities.

Weisskopf units are useful as a comparison point for the measured reduced transition probabilities. If the experimental transition probability is smaller than the Weisskopf estimate, it can be assumed that the nuclear structure differs from simple assumptions. For high transition probabilities there are several particles participating to the transition.

2.3.1 Seniority scheme

The seniority scheme is a model developed to describe semi-magic nuclei that have either magic proton or neutron number [Talmi62]. In the seniority scheme the states are described by the seniority ν, which is the number of nucleons not coupled to $J^\pi = 0^+$ pairs. For even-even nuclei the 0^+ ground-state has always $\nu = 0$. The seniority $\nu = 2$ states are formed by breaking a pair. It is possible for the nucleons of this pair in a particular j shell to form seniority $\nu = 2$ states with spin and parities of 2^+, 4^+... $(2j+1)^+$. All of these states would have the same energy in the simplest model. Any residual interaction breaks this degeneracy.

A characteristic sign of the seniority scheme is an almost constant excitation energy of the first 2^+ state across a whole j shell. Also, the binding-energy difference between even and odd nuclei can be related to the seniority of the ground states. A good example of seniority-like structures are the excitation energies of 2^+ states in tin isotopes. They are almost constant between the magic numbers $N = 50$ and $N = 82$ [Guastalla13, Ekström08, Banu05, Cederkäll07]. The excitation energies and reduced transition probabilities of the heavy polonium nuclei like ^{210}Po with two protons above the $Z = 82$ closed shell and $N = 126$ can be well described within the seniority scheme [Ellegaard73].

Seniority predicts different reduced transition probabilities for seniority-conserving and non-conserving transitions. Instead of predicting absolute transition probabilities, seniority scheme is normally used to predict and compare transition probabilities of different transitions in the same nucleus or between neighboring nuclei.

The matrix elements for an $E2$ transition, which does not conserve seniority, of two nuclei with valence nucleons at j orbit can be related by

$$\langle j^n\, \nu\, J|\, |E2|\, |j^n\, \nu - 2\, J'\rangle = \frac{(n-\nu+2)(2j+3-n-\nu)}{2(2j+3-2\nu)}\, \langle j^\nu\, \nu\, J|\, |E2|\, |j^\nu\, \nu - 2\, J'\rangle\,, \tag{2.12}$$

where n is the number of nucleons in the shell. The $2^+ \rightarrow 0^+$ transitions never conserves the seniority. This gives for the reduced transition probability $B(E2; 2^+ \rightarrow 0^+) \propto n\left(1 - \frac{n}{2j}\right)$ for $j >> 1$. This smooth behavior of the reduced transition probabilities has been observed for tin isotopes with $N > 66$ [Jungclaus11].

For seniority conserving $E2$ transitions the matrix elements of nuclei with different number of valence particles can be related by

$$\langle j^n\, \nu\, J|\, |E2|\, |j^n\, \nu\, J'\rangle = \frac{2j+1-2n}{2j+1-2\nu}\, \langle j^\nu\, \nu\, J|\, |E2|\, |j^\nu\, \nu\, J\rangle\,. \tag{2.13}$$

For the seniority non-conserving transitions the maximum in reduced matrix elements is at midshell with $n/j = 0.5$. The seniority-conserving transitions

reach the minimum value at midshell. This behavior is unique to the seniority scheme and can be used to to predict shell closures from the measured transition probabilities.

2.4 Collective excitations

Far from the closed shells, the interactions between the protons and neutrons distort the spherical shape and enable deformation. The nuclear shape can be described with spherical harmonics $Y_{\lambda\mu}(\theta, \phi)$ and a time dependent-amplitude $\alpha_{\lambda\mu}(t)$:

$$R(t) = R_{\text{av}} + \sum_{\lambda \leq 1} \sum_{\mu=-\lambda}^{+\lambda} \alpha_{\lambda\mu}(t) Y_{\lambda\mu}(\theta, \phi). \tag{2.14}$$

The most common mode of deformation is the symmetric quadrupole deformation with $\lambda = 2$ and $\mu = 0$. Also, octupole deformation with $\lambda = 3$ has been observed, for example in radium and barium nuclei [Gaffney13, Bucher16].

The quadrupole deformation in an axially symmetric nucleus is normally described with a deformation parameter β,

$$\beta = \frac{4}{3}\sqrt{\frac{\pi}{5}}\frac{\Delta R}{R_{\text{av}}}, \tag{2.15}$$

where ΔR is the maximum difference of the semimajor and semiminor axes of the ellipsoid and R_{av} is the average radius. Nuclei with $\beta > 0$ are prolate deformed and $\beta < 0$ oblate deformed.

2.4.1 Vibrational excitations

As indicated by the time-dependence of $\alpha_{\lambda\mu}(t)$ in equation 2.14, it is possible for a nucleus not to have a constant shape. If the coordinates change in a harmonic fashion, the nucleus vibrates around an equilibrium shape. Such

vibrational states can be described in terms of vibrational phonons. The most common vibrational excitations of a spherical nucleus are formed by creating a quadrupole (angular momentum $\lambda = 2$) phonon. Thus the spin and parity of the first vibrational state in a spherical even-even nucleus is normally 2^+. With two quadrupole phonons, three states with spin and parity of 0_2^+, 2_2^+ and 4_1^+ can be created. With fusion-evaporation reactions (see section 3.1) the yrast 4^+ member of the triplet is the easiest to observe. The vibrational model predicts the energy ratio $E(4_1^+)/(2_1^+) = 2$. The $^{114-118}$Te isotopes are the best examples of such spherical vibrational nuclei [Luukko69].

For spherical vibrations the electric transition probability from the ground state to the one-phonon vibrational state can be written as [Bohr98]

$$B(E\lambda : n_\lambda = 0 \rightarrow n_\lambda = 1) = \left(\frac{3}{4\pi} ZeR\right)^2 \beta_{\mathrm{rms}}^2, \tag{2.16}$$

where β_{rms} is the root-mean square of the deformation and R the equilibrium radius. The more general situation can be written with the sum rule [Bohr98]

$$\sum_{J_{n-1}} B(E\lambda : n_\lambda J_n \rightarrow n_\lambda - 1 J_{n-1}) = n_\lambda B(E\lambda : n_\lambda = 1 \rightarrow n_\lambda = 0), \tag{2.17}$$

where the total reduced transition probability is divided to several J_{n-1} states.

Combining these gives $B(E2; 4^+ \rightarrow 2^+)/B(E2; 2^+ \rightarrow 0^+) = 2.0$ for a spherical vibrational nucleus. Normally the reduced transition probabilities are of the order of 10-100 W.u. for the $E2$ transitions connecting the lowest spherical vibrational states.

2.4.2 Rotational excitations

A nucleus with static deformation can also rotate. In the simple model the quadrupole deformation ($\lambda = 2$ and $\mu = 0$ in equation 2.14) of the nucleus stays constant and the excitation energy is generated by the rotation. Here

only rotation of even-even nuclei with bands that have no angular momentum projection to the symmetry axis ($K = 0$) are considered.

In analogue with classical rotation, the energies of the states in a rotational band can be written as

$$E(J) = \frac{\hbar^2}{2\mathcal{J}} J(J+1), \tag{2.18}$$

where $\mathcal{J}$ is the moment of inertia for the nucleus. Only even values for the spin J are allowed. Rotational bands with nearly constant moment of inertia can be found in the regions of well-deformed nuclei. One such region is the rare-earth region around ^{170}Er.

For an axially symmetric rotating nucleus the electric quadrupole moment Q_0 is constant for all of the states,

$$Q_0 = \frac{16\pi}{5} \langle J\,\xi |\, |E2|\, |J\,\xi\rangle\,. \tag{2.19}$$

The reduced transition probability in the equation 2.11 can be related to the transition quadrupole moment Q_t by [Bohr98]

$$B(E2; J_i \to J_f) = \frac{5}{16\pi} e^2 Q_t^2 \langle J_i 020 | J_f 0\rangle^2\,. \tag{2.20}$$

If the nucleus is a rigid rotor then $Q_0 = Q_t$. Inserting the Clebsch-Gordan coefficients gives $B(E2; 4^+ \to 2^+)/B(E2; 2^+ \to 0^+) = 1.21$ for the first excited states in the rotational band. For the $E2$ transitions between high-spin states the $B(E2)$ values are almost constant.

The quadrupole moment can be used to calculate an approximation of the deformation with

$$Q_0 = \frac{3}{\sqrt{5\pi}} R_{\mathrm{av}}^2 Z\beta(1 + 0.16\beta). \tag{2.21}$$

Because only Q_t^2 can be obtained from equation 2.20, the sign of the deformation

parameter has to be obtained by other means.

Chapter 3

Experimental methods

3.1 Fusion-evaporation reaction

Fusion-evaporation reactions enable access to proton-rich nuclei from the valley of β stability to the proton drip line. In a fusion-evaporation reaction the beam and the target nuclei can fuse together to form a highly excited compound nucleus. It is possible for the compound nucleus to either fission or lose the excitation energy and angular momentum by emission of particles and γ rays. In the latter case, the nucleus loses excitation energy first by particle emission. The type and number of emitted particles depend on the neutron-, proton- and alpha-particle separation energies of the compound nucleus. In the region of $N \approx 90$ and $Z \approx 78$ the charged-particle evaporation channels are highly favored. When particle emission is no longer energetically favorable but the nucleus is still highly excited, emission of statistical $E1$ γ rays proceeds carrying away energy but little angular momentum.

The states with the lowest excitation energy for a given angular momentum are called yrast states. These are also the most common discrete states that can be observed via fusion-evaporation reactions.

Lifetimes of the excited states vary from the femtosecond range for collective states with high angular momentum down to the nanosecond range for lower

Table 3.1. In the present experiments, ^{92}Mo (^{78}Kr, $2p/2p2n$) $^{168/166}$Os fusion-evaporation reactions were used. The beam energy, target and magnesium degrader thickness for measurements of lifetimes are summarized.

Experiment	Beam energy (MeV)	Target thickness ($\mathrm{mg\,cm^{-2}}$)	Degrader thickness ($\mathrm{mg\,cm^{-2}}$)
^{166}Os level scheme	357	1.0	-
^{166}Os level scheme, part 2	368	1.0	-
^{166}Os lifetimes	380	0.5	1.0
^{168}Os lifetimes	345	1.0	1.0

lying states. For isomeric states lifetimes up to seconds or longer are possible. These long lifetimes are caused by small transition energy, large multipolarity of the transition or a change in the nuclear structure.

Due to the kinematics of fusion-evaporation reactions the recoils are mainly forward focused. The angular spread of the recoiling nuclei depends on the beam energy and evaporation channel, but is generally small compared to transfer reactions or Coulomb excitation. No particle detection is necessary to correct for the Doppler shift in the energy of the emitted γ rays. Moreover, the small angular spread of the ions enables high transmission efficiency for recoil separators enabling recoil gating and recoil-decay tagging for identification of the reaction products, see section 3.5.

In the experiments described in this work, fusion-evaporation reactions have been used with a ^{78}Kr beam and a ^{92}Mo target. For lifetime experiments a magnesium degrader was used to slow down the recoils. The details of different experiments have been summarized in table 3.1.

3.2 Timing

There are several different techniques to measure lifetimes of excited states of nuclei. A schematic overview of different lifetimes accessible with different methods is presented in figure 3.1.

With large germanium detectors lifetimes down to a few nanoseconds are

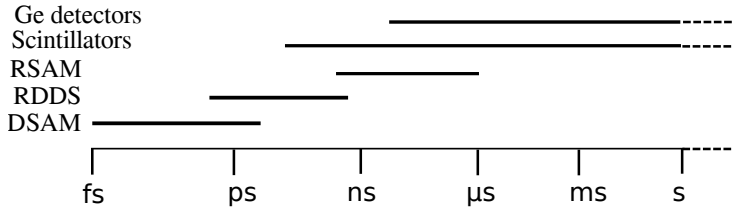

Figure 3.1. Different timing methods for different lifetimes of excited states. For longer lifetimes direct measurement with germanium detectors or for shorter lifetimes, scintillator detectors, is possible. For shorter lifetimes, indirect methods are required. Recoil Shadow Anisotropy Menthod (RSAM) employs the solid angle effects of the set-up. The Recoil Distance Doppler-Shift (RDDS) method and Doppler-Shift Attenuation method (DSAM) are based on the γ-ray energy dependence on velocity of the nucleus, due to the Doppler effect. They use metallic foils to slow down the recoil and shift the γ-ray energy. Instead of time, the distance traveled by the nucleus is measured.

reachable in direct timing measurements. The constricting limit is the time resolution of the detector. Scintillator detectors with faster rise times, like $LaBr_3$ or BaF_2, enable lifetime measurements down to tens of picoseconds [Lica16]. These types of measurements are commonly called fast timing measurements. Direct measurement of the time difference between the γ rays also enables measuring lifetimes of states fed by isomers.

For shorter lifetimes indirect measurements are required. In the Recoil Shadow Anisotropy Method (RSAM) [Gueorguieva01] the lifetime is obtained from the change in the effective detector solid angle when the nucleus decays in-flight away from the direct view of the detector. The measurement is based on the solid-angle suppression of the heavy-metal collimators used with the Compton-suppression shields. The measurable lifetimes depend on the recoil velocity and the geometry of the detector set-up.

The Recoil Distance Doppler-Shift (RDDS) method [Alexander65, Dewald12] and Doppler-Shift Attenuation method (DSAM) [Branford73] are both based on the Doppler shift of the measured γ-ray energies. With RDDS, lifetimes of the order of picoseconds to nanoseconds can be measured but the feeding states have to have shorter lifetimes than the states of interest. With DSAM the nuclei are slowed down and eventually stopped in a thick target or the backing of the target. The line shape of the measured γ-ray peak depends on

the lifetime of the excited state and the energy-loss of the nucleus in medium. With the DSAM method, lifetimes shorter than picoseconds can be reached.

3.2.1 The Recoil Distance Doppler-Shift method

The measured γ-ray energy depends not only on the transition energy E_0, but also on the velocity of the nucleus. For small velocities with respect to the speed of light, the measured energy can be written as

$$E_\gamma \approx E_0 \left(1 + \frac{v}{c} \cos\theta\right), \tag{3.1}$$

where v is the speed of the nucleus, c is the speed of light and θ is the angle between the velocity of the recoiling nucleus and the detector.

In the Recoil Distance Doppler-Shift technique, a plunger device is used to mount a stopper foil behind the target to stop the recoiling nuclei. This is illustrated in figure 3.2 a. Often a thick gold foil is used as a stopper. The measured energy allows determination, whether the γ ray was emitted before the nucleus slowed down or after it stopped in the stopper. Usually the γ rays emitted before the stopper are called shifted as their energy is shifted with respect to the transition energy (if the detector is not mounted at $\theta = 90°$). The peak they form in the spectrum is normally called shifted peak. The γ-ray peak due to emission when the nucleus is already stopped is, unsurprisingly, called the unshifted or stopped peak.

If the reaction products of interest have a small cross section compared to other reaction channels, it is necessary to identify them in order to reduce the background from other γ rays. To enable this, the classical stopper method can be modified by replacing the stopper with a degrader, which slows the nuclei down and enables them to pass through for subsequent identification. The situation is illustrated in 3.2 b. The degraded γ rays have energy $E' = E'(v')$ according to equation 3.1.

The material of the degrader and its thickness is a compromise. The nuclei have to slow down sufficiently to obtain a large enough energy difference, $E_{\text{shifted}} - E_{\text{degraded}}$. The areas of the shifted and degraded peaks are used

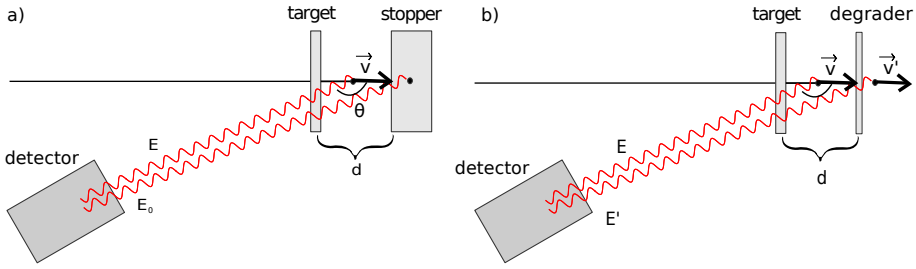

Figure 3.2. The RDDS method employs the γ-ray energy depends not only on the transition energy E_0, but also on the velocity of the nucleus and the angle of the detector. a) In the traditional plunger set-up the nucleus is stopped inside the stopper which is a distance d after the target. The measured γ-ray energy allows the deduction, whether the decay happened before the nucleus was stopped or not. b) The set-up can be modified by replacing the stopper foil by a degrader, which slows down the nucleus and allows it to pass through. This enables the nuclei to travel downstream for the subsequent identification.

for the analysis and have to be determined accurately. The energy difference depends on the transition energy, velocity change and the angle between the recoil velocity and the detector. If the detectors are placed close to $\theta = 0°$ or $\theta = 180°$, a smaller change in the velocity of the nucleus is required. Furthermore, since a thicker degrader increases scattering and reduces the transmission of the nuclei, it must be kept as thin as possible. Finally, due to the possiblity of Coulomb excitation of the degrader material, isotopes with no strong collective bands at low energies are favored.

With the set-up used in this work, the $1\,\mathrm{mg/cm^2}$ Mg foil was seen to reduce the transmission of the RITU separator (see section 3.3.2) by a factor of 2/3. Higher Z materials have been tested earlier, but the best transmission of RITU was obtained with magnesium [Grahn08]. Also the small collectivity of the excited states reduces the Coulomb-excitation probability.

The fraction of the unshifted component is

$$I'_{\mathrm{u}}(x) = \frac{I_{\mathrm{u}}(x)}{I_{\mathrm{s}}(x) + I_{\mathrm{u}}(x)}, \tag{3.2}$$

where $I_{\mathrm{u}}(x)$ is the intensity of the unshifted γ rays and $I_{\mathrm{s}}(x)$ the intensity of

the shifted γ rays. It gives the fraction of the nuclei that have yet to decay after distance x. The target-to-stopper distances can be converted into times as the velocity of the recoiling nucleus can be obtained with equation 3.1. A very rough estimate for the lifetime of a single state can be obtained with meaurements at a single distance. Using equation 3.2, the measured intensities of the shifted and unshifted γ-ray peaks can be related to the lifetime with the definition of the decay law in equation 2.1. In reality, measurements at several distances are required.

By varying the target-to-stopper distance and fitting the shifted and unshifted components of the γ rays under study for each distance, a decay curve can be formed by plotting the normalized fraction of the unshifted component (equation 3.2) against distance (time). The intensities can also be externally normalized. A commonly used normalization is obtained from the strongest transitions in the yrast band. The shape of the decay curve should not depend on the used normalization. The fitted areas for the $2^+ \rightarrow 0^+$ transition in ^{166}Os is presented in 4.6 with the fitted decay curve.

In the case of only one single state, the lifetime can be obtained by fitting an exponential function to the decay curve. For multiple states, the Bateman equations (equation 2.4) can be used. In practice, almost all of the analysis is done with the Differential Decay Curve method (DDCM), see section 3.6. With DDCM the individual lifetimes can be analyzed separately without taking the structure of the feeding states into account beyond those directly feeding the state of interest.

3.2.2 The Recoil Shadow Anisotropy method

The Recoil Shadow Anisotropy method is a method suitable for measuring lifetimes of the order of nanoseconds [Gueorguieva01]. It is based on the change in the detector solid-angle when the nucleus emits the γ ray at a distance x behind the target position. The situation is illustrated for Jurogam II in figure 3.3. If the γ ray is emitted at the target position, the solid angles for both of the clover detectors around $\theta = 90°$ are the same, as are the solid angles for the individual crystals. This analysis excludes relativistic effects, as the velocity of the nuclei is $0.03c$ after the degrader.

If there is an isomeric state in the nucleus, the decay can happen a short distance after the target. In this case the solid angles of the detectors are not the same anymore. The change in the solid angle is caused by the shadowing effect of the heavy-metal collimators of the Compton-suppression shields.

The shadowing effect is more pronounced in the clover crystals on the downstream side, as seen from figure 3.3 b.

The observed anisotropy can be written as

$$A_\gamma = \frac{I_\gamma(\theta = 71°) + I_\gamma(\theta = 100°) - I_\gamma(\theta = 80°) - I_\gamma(\theta = 109°)}{I_\gamma(\theta = 80°) + I_\gamma(\theta = 109°) + I_\gamma\theta = 71°) + I_\gamma(\theta = 100°)} \tag{3.3}$$

with the intensities I_γ observed at different detector angles. For a fast transition this anisotropy will vanish. The asymmetry in equation 3.3 is constructed in a symmetric manner around $\theta = 90°$ and hence to first order the effect of angular distributions should vanish.

For a given energy, the relative difference in the detection efficiencies $\Delta\epsilon$ as a function of distance behind the target can be written as

$$\Delta\epsilon(x) = \frac{\epsilon_{\theta=80°}(x) + \epsilon_{\theta=109°}(x) - \epsilon_{\theta=71°}(x) - \epsilon_{\theta=100°}(x)}{\epsilon_{\theta=80°}(x) + \epsilon_{\theta=109°}(x) + \epsilon_{\theta=71°}(x) + \epsilon_{\theta=100°}(x)}. \tag{3.4}$$

With this, the anisotropy for the γ ray can be written as

$$A_\gamma = \int_0^\infty \Delta\epsilon(x)\epsilon_0(x)P_\gamma(t)\mathrm{d}t, \tag{3.5}$$

where $\epsilon_0(x)$ is the total detection efficiency and $P_\gamma(t)$ is the probability that the γ ray is emitted at time t. Assuming that the feeding of the state of interest is fast, the probability of the decay can be written with the decay law giving

$$A_\gamma = \int_0^\infty \frac{1}{v}\Delta\epsilon(x)\epsilon_0(x)\lambda \mathrm{e}^{-\lambda\frac{x}{v}}\mathrm{d}x. \tag{3.6}$$

Integration of 3.6 gives a calibration curve for the decay constant as a function

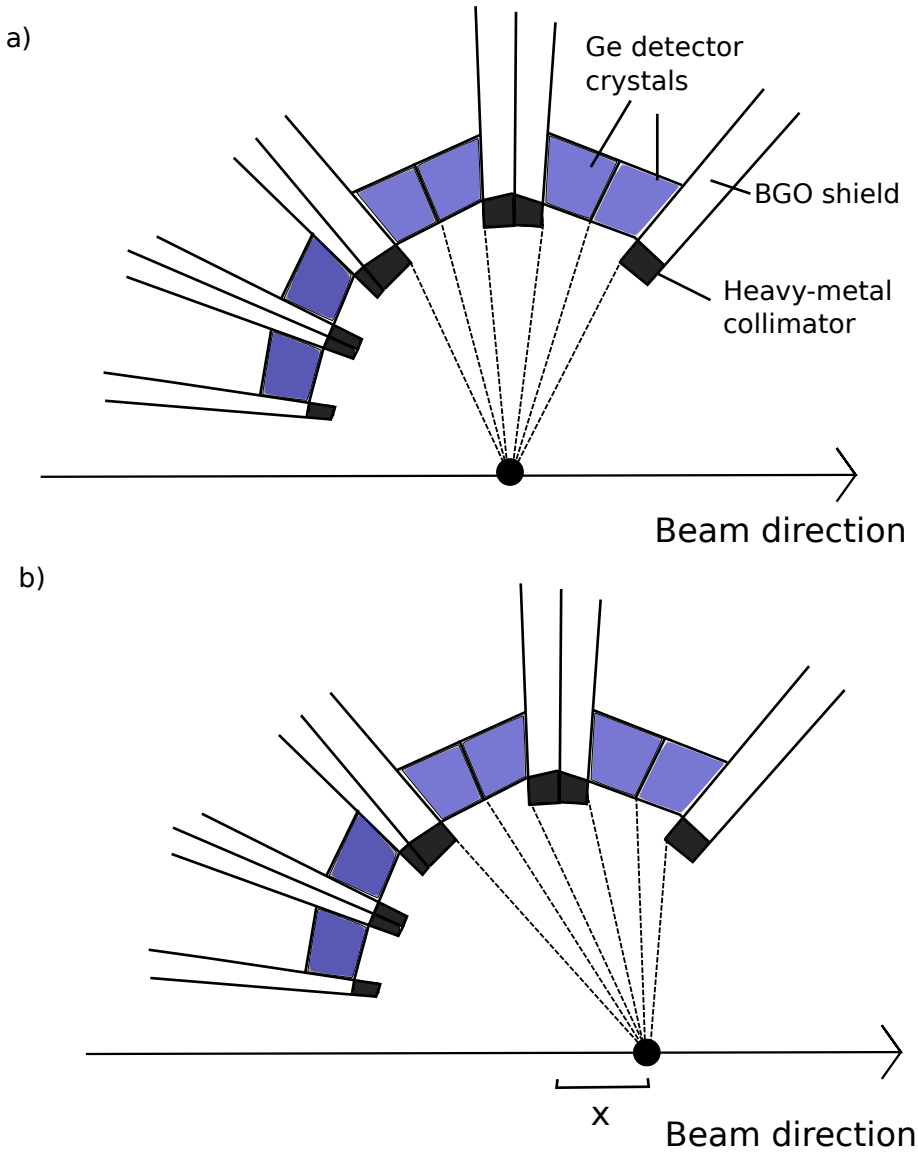

Figure 3.3. The geometry of the Jurogam II germanium-detector array. The detectors are set into rings with Phase1 or GASP type detectors in the backward angles and clover detectors around $\theta = 90°$. a) If the γ ray is emitted at the target position the solid angles for all of the detectors are identical. b) If the γ ray is emitted at a distance x behind the target the solid angles are no longer the same for all of the crystals. The forward-positioned crystals of both clover rings are shadowed by the heavy-metal collimator of the Compton-suppression shields.

of the measured γ-ray asymmetry.

3.3 Experimental set-up

3.3.1 Jurogam I and II

In the present work, prompt γ rays at the target position were detected with two different germanium-detector set-ups, Jurogam I and its successor Jurogam II. Both of them consist of high-purity germanium detectors. Germanium is used to detect γ rays due to its good energy resolution and reasonably high efficiency for detection. A germanium detector is a semiconducting diode, where high voltage of $3-4\,\mathrm{kV}$ is used to deplete the crystal and to collect the electron-hole pairs induced by γ rays ionizing the depleted region. To enable the use of the high voltage, the detectors are kept cold with liquid nitrogen. For the 1.3 MeV γ rays from ^{60}Co the obtained full-width at half maximum (FWHM) varies from $2-3.5\,\mathrm{keV}$ for the detectors in the array.

Every detector is surrounded by a Compton-suppression shield made of Bismuth Germanite (BGO). The purpose of the shield is to veto those gamma-rays that do not leave all of their energy in the germanium crystal, but instead Compton scatter and deposit some of their energy in the shield. Bismuth has $Z = 83$ and thus the shield has high efficiency for detecting γ rays. If a γ ray is detected within a short time overlap in the detector and its shield, it can be marked in the data as Compton scattering and disregarded later. With Compton suppression, the number of γ rays on the photo peak compared to the number of γ rays in the spectrum (known as the peak-to-total ratio) can be increased from 0.15 to 0.5. Heavy-metal collimators are used in front of the shields to eliminate γ rays interacting only with the shield.

Jurogam I consists of 43 coaxial detectors of either GASP [Alvarez93] or Eurogam Phase1 [Beausang92] type. They are placed into six rings and every ring has a fixed angle θ with respect to the beam direction. The angles and the number of detectors in each ring are listed in 3.2.

Jurogam II is an upgrade of Jurogam I. Rings 1 and 2 have remained in place but

Table 3.2. The detector angles θ with respect to the beam direction for Jurogam I and Jurogam II. The number of detectors in each ring is also presented. In Jurogam II, rings 3 and 4 are formed by clovers and the given angles are for the center of the clover detector. The angles for the crystals can be obtained by adding or subtracting 4.5°.

Ring	Angle θ	# of detectors
	Jurogam I	
1	157.6	5
2	133.57	10
3	107.94	10
4	94.16	5
5	85.84	5
6	72.05	8
	Jurogam II	
1	157.6	5
2	133.57	10
3	104.5	12
4	75.5	12

the other detectors have been replaced with 24 clover type detectors [Duchêne99] placed into two symmetric rings around $\theta = 90°$. The clover detectors consist of four crystals, each of which is read out separately. This enables an requires the use of the add-back technique. In this technique the γ-ray energies observed in neighboring crystals within a short time interval are added together, as they probably origin from the same γ ray that Compton scatters. The major benefit of the upgrade is higher efficiency caused by the larger detectors in a more compact geometry.

3.3.2 RITU and GREAT

RITU (Recoil Ion Transport Unit) is a gas-filled recoil separator used to separate the fusion-evaporation products from the beam and target-like products. As the vast majority of the beam particles pass through the target without inducing nuclear reactions, it is necessary to separate the reaction products from these uninteresting ions. The combined set-up of Jurogam, RITU and GREAT is presented in figure 3.4.

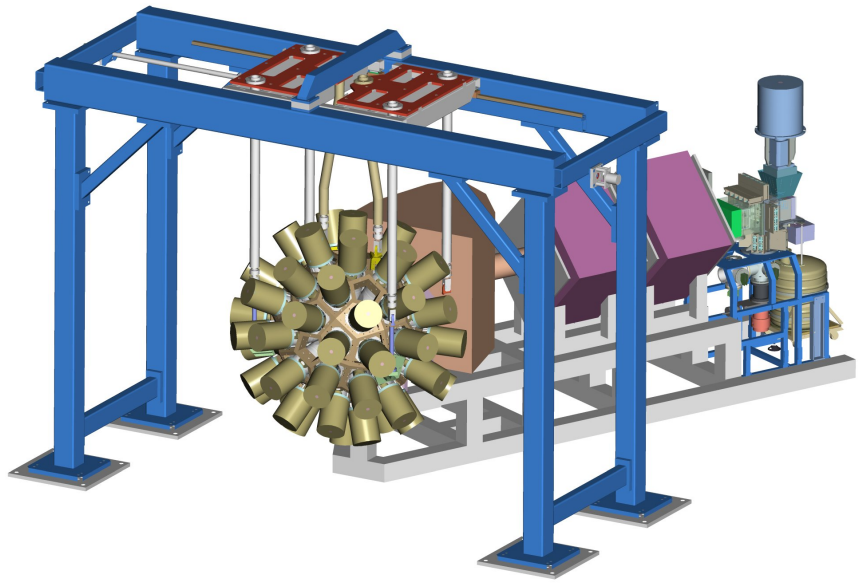

Figure 3.4. The set-up for the experiments consisted of the Jurogam I (in the figure) of Jurogam II Ge-detector array combined to RITU separator and the GREAT spectrometer at the focal plane.

The magnetic components of RITU are a quadrupole, a dipole and a quadrupole doublet. The separation of reaction products from the beam is done with the dipole, and the quadrupoles are used to focus the recoils to the focal plane. RITU is filled with a low-pressure helium gas, typically at 0.5 mbar. This enhances the transmission as all of the recoils have an average charge state as a result from collisions with the gas atoms but suppresses the mass-resolving power of the system. The magnetic rigidity $B\rho$ can be calculated by using the average charge q_{ave}

$$B\rho = \frac{mv}{q_{\mathrm{ave}}}, \tag{3.7}$$

where m is the mass and v the velocity of the ions. The average charge state is different for the beam and the recoils enabling separation. There are several empirical formulas for the charge state, all depending on the atomic number of the ion and the velocity [Bohr40, Oganessian91].

The GREAT (Gamma Recoil Electron Alpha Timing) spectrometer is situated at the focal plane of RITU, where the ions pass through the Multi-Wire Proportional Counter (MWPC) and are implanted into the Double-sided Silicon Strip Detector (DSSD). The time-of-flight between the MWPC and the DSSD and the energy loss in the MWPC are used to distinguish between the recoils and the scattered beam and the target-like products. The DSSD consists of two silicon detectors with 120×40 pixels. It is surrounded by a planar germanium and three clover germanium detectors to detect isomeric γ rays. The flight time through RITU gives a lower limit of approximately 0.5 µs for the lifetimes of isomeric transitions. The upper limit is given by the recoil implantation rate R in the DSSD, $\tau < 1/R$. A high implantation rate prevents clean correlations of a particular implant.

3.3.3 Plunger devices

Lifetimes measured with RDDS are usually of the order of picoseconds. For fusion-evaporation reactions the recoil velocities are typically $0.01 - 0.1\,c$ and thus the relevant distances are $1 - 10\,000$ µm. To measure lifetimes accurately

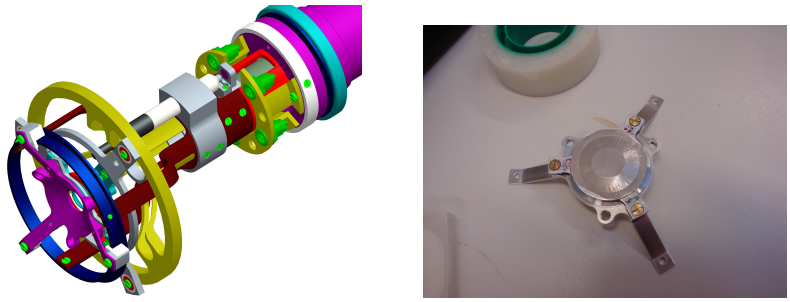

Figure 3.5. a)The mechanics of the DPUNS plunger at the target end. The degrader is glued on the grey frame and stretched over the purple frame. The target is similarly stretched and placed on the upstream side of the degrader. Also the structure to enable precise movement of the target is visible in the figure. b) The target and degrader foils are stretched over cone-like frames to enable accurate distance measurement.

the errors in the determined relative distances have to be well below 1 µm for short distances. It is worth noting that there is no accurate method to determine the absolute target-to-degrader distances with the plunger devices used in the present study. Fortunately, only relative distances are of importance if Differential Decay Curve Method is used for the analysis, see section 3.6.

In the present work, the Cologne plunger [Cleemann78] was used for ^{168}Os and the DPUNS plunger (Differential Plunger for Unbound States in Nuclei) [Taylor13] for ^{166}Os. The design of the devices is almost identical. DPUNS has a lower voltage motor which enables its use in the low-pressure helium and differential pumping system in the RITU gas-filled separator. In the Cologne plunger, a carbon foil is used to isolate the motor from RITU. The carbon foil induces some scattering and removes the cooling effect of the helium on the target and degrader. The design of DPUNS is shown in figure 3.5 a.

As the distances of interest are short, the distance between the target and the degrader foils must be as constant as possible. The foils are stretched on their respective cone-like frames. Normally the degrader is set to the center of the germanium-detector array and the target is moved backwards. Therefore, the target is connected to the motor which is capable of moving with a precision less than 0.1 µm. The distance has to be adjusted when the beam is on target to compensate the changes in the distance induced by the heat. The distance

measurement and adjustment is done automatically by a software. This is crucial for distances shorter than 100 µm and also beneficial for distances shorter than 1000 µm.

The target and degrader foils are aligned. The shortest measurable distance depends on the alignment of the foils, as they need to be electrically insulated for the distance measurement. If the foils are not properly aligned, it is likely that no short distances can be measured as the edges of the frames would be touching each other. Aligning is usually done by eye, as it is so far the most precise method. Optical contact is defined as a point where no light shines between the target and degrader foils. Besides the alignment, the smoothness of the foils determines the minimum distances that can be measured.

The distances are measured during the experiment by an induced voltage from the target to the degrader. The distance calibration is done without the beam on target by measuring the conductance between the foils as a function of distance and comparing it to the distance measured by the micrometer. In practice this is done by feeding a pulser signal to the target and measuring the induced voltage U in the degrader. Mechanical contact is the measured distance x, where the slope of the $(x, 1/U)$ curve changes. This is determined by the alignment and smoothness of the foils. Electric contact is the distance where the foils are so close, that the voltage signal can no longer be measured reliably. Generally, the optical contact represents a longer distance than the mechanical contact, which is once again longer than the electric contact. Only distances longer than the mechanical contact can be measured.

For short distances (< 1000 µm) an automatic software control system is used to adjust and measure the distance. For longer distances, the induced voltage is too small to reliably monitor and control the distance. Fortunately, the accuracy of the micrometer is also enough for these long distances as the relative error is small.

3.4 Data Acquisition

The triggerless Total Data Readout (TDR) [Lazarus01] data acquisition was used. Every channel is read out separately and all of the events are stamped with a 100 MHz metronome giving 10 ns time resolution. For Jurogam II, the analogue electronics of Jurogam I were replaced by digital Lyrtech-ADC cards enabling higher count rates. The events from different channels are time ordered by a dedicated Merge computer and further sent to online sort and to disk. Correlations between decays, recoils and prompt γ-rays are done subsequently in the analysis software.

The data was constructed into correlated events with the Grain software [Rahkila08]. The γ-ray spectra and $\gamma\gamma$ matrices were analyzed with Radware packages [Radford95a, Radford95b].

3.5 Recoil-decay tagging

Recoil-Decay Tagging (RDT) enables associating the prompt γ rays detected at the target position to the recoil and its decay observed with the GREAT spectrometer at the focal plane [Paul95]. The recoils are separated from scattered beam particles and target-like products by their energy loss in the MWPC and time-of-flight between the MWPC and the DSSD. It is possible to use the deposited energy in the DSSD as a gate as well. For charged-particle decays and fission of the implanted recoil, the decay can be assigned to the same pixel of the DSSD where the recoil was implanted. Only decays within a time gate of $3t_{1/2}$ are accepted. It is possible to go on with the decay chain in a similar manner. The second decay should happen in the same pixel within a new time gate $3t'_{1/2}$. In addition, for α decays, the characteristic α-particle energy can be used as a gating condition to limit random correlations. Isomeric γ rays can also be used for tagging [Cullen98], but no spatial correlation is possible. For β decays the continious energy spectrum of the electron (or positron) makes correlations more demanding [Ruotsalainen13].

In this work, recoil-decay tagging has been used to identify the α-decaying ^{166}Os nuclei. Only the α decays happening in the same pixel with the recoil

implantation were taken into account with additional energy and time gates. For ^{168}Os, α decays were used for cleaning the γ-ray spectra but not for $\gamma\gamma$ coincidences due to the small α-decay branching ratio.

3.6 Differential Decay Curme Method

It is difficult to to obtain lifetimes for excited states with complicated feeding patterns using equation 2.4. Not all of the feeding can be observed and by fitting all of the parameters at once, it is hard to disentangle systematic errors. Another problem is the measurement of the absolute target-to-stopper distances. The Differential Decay Curve Method (DDCM) is an alternative approach to obtain the lifetimes. The major benefits are that only measurable quantities are used for obtaining the lifetimes. It is easier to notice systematic uncertainties and only relative distances are required for the analysis. DDCM was introduced by Dewald et al in 1989 [Dewald89]. Lifetimes are obtained separately for every state instead of fitting all of the states at once.

Rewriting the Bateman equation 2.4 for level L_j with levels N L_i feeding it gives

$$\frac{\mathrm{d}}{\mathrm{d}t}n_j(t) = -\lambda_j n_j(t) + \sum_i^N \lambda_i n_i(t) b_{ij}. \tag{3.8}$$

Integrating this from time t to infinity gives

$$\int_t^\infty \frac{\mathrm{d}}{\mathrm{d}t}n_j(t)\mathrm{d}t = \underbrace{-\lambda_j \int_t^\infty n_j(t)\mathrm{d}t}_{R_j(t)} + \sum_i^N \underbrace{\int_t^\infty \lambda_i n_i(t) b_{ij}\mathrm{d}t.}_{R_{ij}(t)} \tag{3.9}$$

$R_j(t)$ is the decay function of level L_j and $R_{ij}(t)$ is the normalized decay function for level L_i and they give the number of the decays after time t. In RDDS measurements they are proportional to the areas of the unshifted components of the corresponding transitions, when t is the time it takes for the recoil to reach the stopper or degrader. Equation 3.9 can be rewritten as

$$n_j(\infty) - n_j(t) = -R_j(t) + \sum_i^N R_{ij}(t). \tag{3.10}$$

Assuming that all of the lifetimes are finite $n_j(\infty) = 0$. The derivative of the decay function R_j can be used to rewrite $n_j(t)$, as $R_(t) = \int_t^\infty n_j(t)\mathrm{d}t$. Thus the lifetime is

$$\tau_j = \frac{1}{\lambda_j} = \frac{R_j(t) - R_{ij}(t)}{\frac{\mathrm{d}}{\mathrm{d}t}R_j(t)}. \tag{3.11}$$

The lifetime and the decay constant can be calculated for any time t separately.

The decay functions can be replaced with the intensities I of the unshifted components by taking the efficiency of the detectors and the angular distribution of the γ rays. Also the times can be easily replaced by distances using the recoil velocity v:

$$\tau_j(x) = \frac{1}{v}\frac{I_j^{\mathrm{u}}(x) - \sum\limits_i b_{ij}\alpha(x)\frac{\epsilon_i\omega_i}{\epsilon_j\omega_j}I_i^{\mathrm{u}}(x)}{\frac{\mathrm{d}}{\mathrm{d}x}I_j^{\mathrm{s}}(x)}. \tag{3.12}$$

Here, the coefficients ϵ and ω normalize the probability of observing the γ rays with regard to the detector efficiency and the angular distribution of the γ-ray transitions. Normally $\omega_i/\omega_j \approx 1$ within the error bars of the measured intensities. A normalization coefficient $\alpha(x)$ is required to normalize the statistics measured at different distances. Equation 3.12 is used for obtaining lifetimes from γ ray singles spectra, if the statistics are not enough to enable coincidence analysis.

By fitting a function to the shifted and unshifted intensities, also the derivative $\frac{\mathrm{d}}{\mathrm{d}x}I_j^{\mathrm{s}}(x)$ can be obtained. As the function is only used to obtain the derivative and it is not related to any physical quantity, any form can be used. Normally smoothly connected second order polynomials are used for fitting these curves as they are easy to use. Both $I_j^{\mathrm{u}}(x)$ and $\frac{\mathrm{d}}{\mathrm{d}x}I_j^{\mathrm{s}}(x)$ are fitted using a function and its derivative with χ^2 analysis. The lifetime can be separately extracted for every measured distance. Usually, the final result is a mean of the single values obtained for the measured distances within the region of sensitivity, defined

as a region where both the numerator and denominator of equation 3.12 are larger than zero. It is also the region inside which the statistical uncertainties of the lifetime are the smallest. Large deviations in the lifetime for short or long distances can indicate systematic errors, usually due to unobserved feeding.

Employing $\gamma\gamma$ coincidences in the analysis is the easiest way to solve the side-feeding problem. The main requirements are a large enough cross section (order of 1 mbarn) and an efficient detector system. The best results are achieved by gating only with the shifted component of the feeding transition [Petkov01]. In this case, equation 3.12 simplifies to

$$\tau(x) = \frac{1}{v} \frac{I^{\mathrm{u}}(x)}{\frac{\mathrm{d}}{\mathrm{d}x} I^{\mathrm{s}}(x)}, \tag{3.13}$$

where the intensities are of the depopulating transition. This is also the only gating method that removes the effects of deorientation (see section 3.6.1) from the analysis. The downside is that the gate has to be clean. This requires that the detectors used for gating have suitable angle θ and the transition energy is high enough to enable gating with only the shifted component. An alternative is to use the degraded component of the depopulating transition for gating but this does not remove the effect of the side feeding.

If the experimental setup does not enable gating with only the shifted component, other gates can be used. In this case $\gamma\gamma$ coincidences are used to select feeding but deorientation is still present. One of the gating methods in the present work is gating with the full line shape of the feeding transition. The time behavior of the feeding transition is obtained by gating with the depopulating transition. This gives a similar equation to 3.12, as gating is used to choose the feeding only. As the analysis only employs events in which both the feeding and depopulating γ rays are detected, the detection efficiencies of the γ rays are not needed, if one can assume that efficiencies of the shifted and degraded components are the same. Therefore, it is only necessary to normalize the statistics measured at different distances. For this, the number of produced nuclei can be used. In practice it can be done with the intensities of the strongest γ-ray peaks in the spectrum (normally the lowest transitions of the yrast line) or by normalizing the transitions by themselves. This gives

$$\tau_j(x) = \frac{1}{v} \frac{I_j^{\mathrm{u}}(x) - \alpha(x) I_i^{\mathrm{u}}(x)}{\frac{\mathrm{d}}{\mathrm{d}x} I_j^{\mathrm{s}}(x)}. \tag{3.14}$$

where $\alpha(x)$ is the normalization coefficient. For relative intensities the lifetime can be written as

$$\tau_j(x) = \frac{1}{v} \frac{\frac{I_j^{\mathrm{u}}(x)}{I_j^{\mathrm{u}}(x)+I_j^{\mathrm{s}}(x)} - \frac{I_i^{\mathrm{u}}(x)}{I_i^{\mathrm{u}}(x)+I_i^{\mathrm{s}}(x)}}{\frac{\mathrm{d}}{\mathrm{d}x} \frac{I_j^{\mathrm{s}}(x)}{I_j^{\mathrm{u}}(x)+I_j^{\mathrm{s}}(x)}}. \tag{3.15}$$

3.6.1 Deorientation

Deorientation affects the nuclear alignment during the flight of the recoils in the vacuum (or in gas) after exiting the target [Goldring82]. In heavy-ion, fusion-evaporation reactions, the spins of nuclei are aligned perpendicular to the beam axis. During the flight through the target, the nuclei lose multiple electrons due to collisions with the target atoms. After the target, the electrons de-excite to energetically favored states creating strong magnetic hyperfine fields. The nuclear spin interacts with these fields changing its direction and losing its orientation. This can be seen for low-spin states where the change is more pronounced.

If the nuclei are in helium gas instead of vacuum, the gas pressure has an effect on the deorientation. For low-pressure gas the effect is usually more pronounced [Brenn77].

In the lifetime analysis, deorientation causes changes in $I_\theta(x)$ as the angular distributions change over time. For the $E2$ transitions, deorientation seems to shorten lifetimes [Petkov95, Dewald12], as the angles used for the analysis are close to 0° or 180°. One way to observe deorientation is to look at $I^s_{\theta 1}(x)/I^s_{\theta 2}(x)$ as the effect depends on the observation angle [Petkov92]. Figure 3.6 shows this ratio for shifted components measured at $\theta = 133.57°$ and $\theta = 72.05°$ for the strongest transitions is ^{166}Os. The observed decreasing trend is consistent with $E2$ transitions and deorientation. The ratio of the shifted components appears to remain constant at large distances, which are in the region of sensitivity for

the transitions of interest, but the error bars are too large for any conclusions.

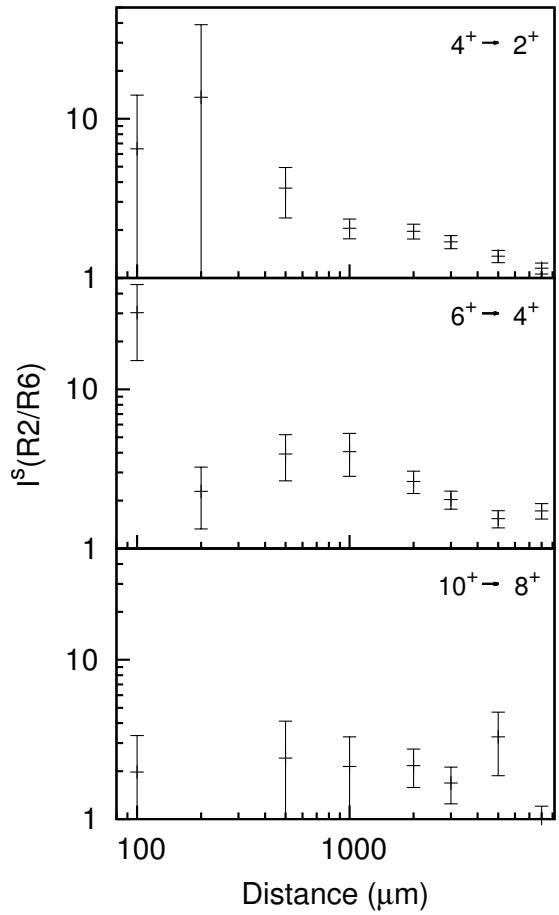

Figure 3.6. The measured γ-ray intensity ratio for the shifted component for Jurogam II rings R2 ($\theta = 133.57°$) and R6 ($\theta = 72.05°$) as a function of target-to-degrader distance for $4^+ \rightarrow 2^+$, $6^+ \rightarrow 4^+$ and $10^+ \rightarrow 8^+$ transitions in ^{166}Os.

Chapter 4

Results

4.1 ^{166}Os

The excited states of ^{166}Os have been studied earlier in two experiments carried out in Jyväskylä. The first experiment was performed by King et al [King00] who discovered the yrast states up to the 8^+ state in an α-decay correlated γ-ray spectrum. The excited states were re-measured by Appelbe et al [Appelbe02]. The yrast sequance was extended up to the 14^+ state and the first states of a negative-parity band were discovered.

4.1.1 Level scheme

In the present work, ^{166}Os was strongly populated as a side product in an experiment dedicated to study the excited states of ^{166}Ir. In order to optimize the yield of ^{166}Ir, two different beam energies were used. The details of the experiment are summarized were table 3.1. The first part with lower beam energy provided cleaner conditions for ^{166}Os as less charged-particle evaporation channels were open. However, in order to obtain more statistics, also the second part of the experiment with higher beam energy was finally included in the analysis.

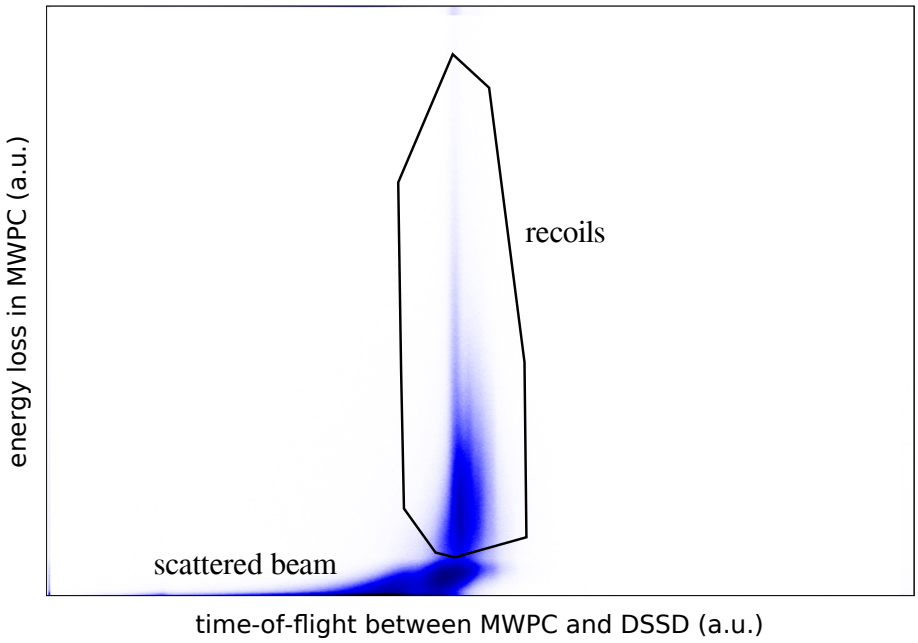

Figure 4.1. The time-of-flight between the multiwire proportional counter and the DSSD plotted against the energy loss in the MWPC. The gate used for identification of the recoils is marked.

The recoils were separated from the scattered beam and target-like products by their time of flight (TOF) between the MWPC and the DSSD and their energy loss (dE) in the MWPC. The TOF-dE matrix and the gate used for recoil identification are presented in figure 4.1.

The ^{166}Os nuclei were identified by employing recoil-decay tagging. The α-decay branching ratio is 60% of the total decay of ^{166}Os. The α-particle energy $E_\alpha = 5.996\,\mathrm{MeV}$ and half-life $t_{1/2} = 213\,\mathrm{ms}$ [Baglin08] provide good tagging conditions. Most of the other nuclei produced in ^{78}Kr+^{92}Mo reactions decay via β decay, making the α-decay tagging of ^{166}Os easier. In figure 4.2, the energy spectrum of the events detected in the same DSSD pixel with the recoil implantation within a search time of 700 ms is shown.

The search time for the α decay has to be long enough to obtain sufficient statistics. However, in order to avoid random correlations due to several recoils hitting the same pixel, it must not be too long. A search time of 700 ms was used

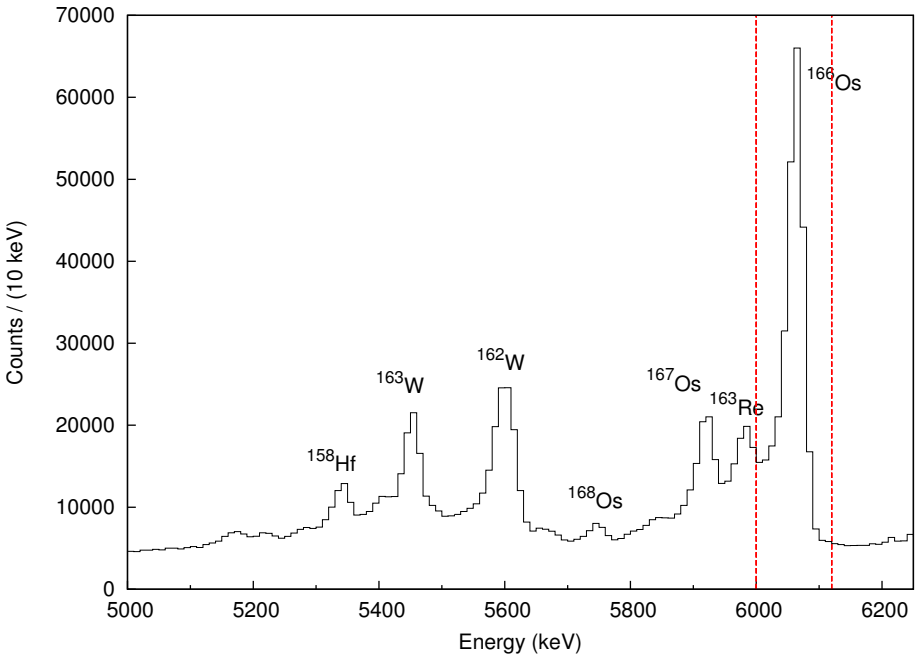

Figure 4.2. The α-particle energy spectrum for decays detected within 700 ms in the same DSSD pixel with the recoil implantation. The strongest peaks are labeled. The energy gate used for selecting ^{166}Os nuclei is marked.

(roughly $3t_{1/2}$) for the α decay of ^{166}Os. Also events in which the α particle escaped the detector leaving only a fraction of its energy, but the full energy of the daughters α decay was detected, were marked as ^{166}Os. The search time for the daughter α decay was two half-lives, 2.8 s.

Because the count rate in the DSSD was 1 kHz, shorter search times of 300 ms and 400 ms were also tested. The resulting Jurogam spectra and matrices were used for checking the $\gamma\gamma$ coincidences. No contaminant peaks were identified among those assigned to ^{166}Os.

Gamma rays detected in Jurogam $0.4 - 0.55$ µs before the recoil was detected in the MWPC were associated with that recoil, corresponding to the expected flight time through RITU. If the recoil was identified to be ^{166}Os and the γ rays were detected within a 100 ns mutual coincidence gate, the γ rays were sorted into a symmetric $\gamma\gamma$ matrix with the Grain software [Rahkila08] and further analysed with the RADWARE ESCL8R software [Radford95a, Radford95b]. The resulting level scheme is presented in figure 4.3 and the identified γ rays are listed in table 4.1. The $\gamma\gamma$ coincidences, intensities and energy and intensity sums have been used to place the γ-ray transitions into the level scheme.

During the eight days with the beam on target, a total of 1.6×10^6 $\gamma\gamma$ coincidences were correlated with the ^{166}Os α decays. The projection of the matrix is shown in figure 4.4 a. Most of the transitions found by King et al. [King00] and Appelbe et al. [Appelbe02] are clearly visible in the spectrum.

Gating with the 626 keV $2349 \rightarrow 1723$ keV γ-ray transition (figure 4.4 b) shows the yrast sequence. Because there is a 625 keV transition in band 5, some of the strongest transitions of bands 4 and 5 are weakly visible in the spectrum. Due to the intensities of the 510 keV and 657 keV γ-ray transitions, the ordering of these transitions has been changed from that suggested by Appelbe et al. Unfortunately, the 2859 keV (10^+) state was not populated strongly enough for $\gamma\gamma$ coincidences to check the decay curve of the 510 keV γ-ray transition in order to confirm this assignment. Analysis of the single γ-ray spectra would not be enough due to the 509 keV $3309 \rightarrow 2800$ keV transition.

In figure 4.4 c, the γ-ray spectrum gated with 811 keV γ-rays is shown. Two new γ-ray transitions of 780 keV and 811 keV were discovered to feed the 6^+ state at 1723 keV. By comparing the decay curves of the 626 keV, 704 keV and 204 keV

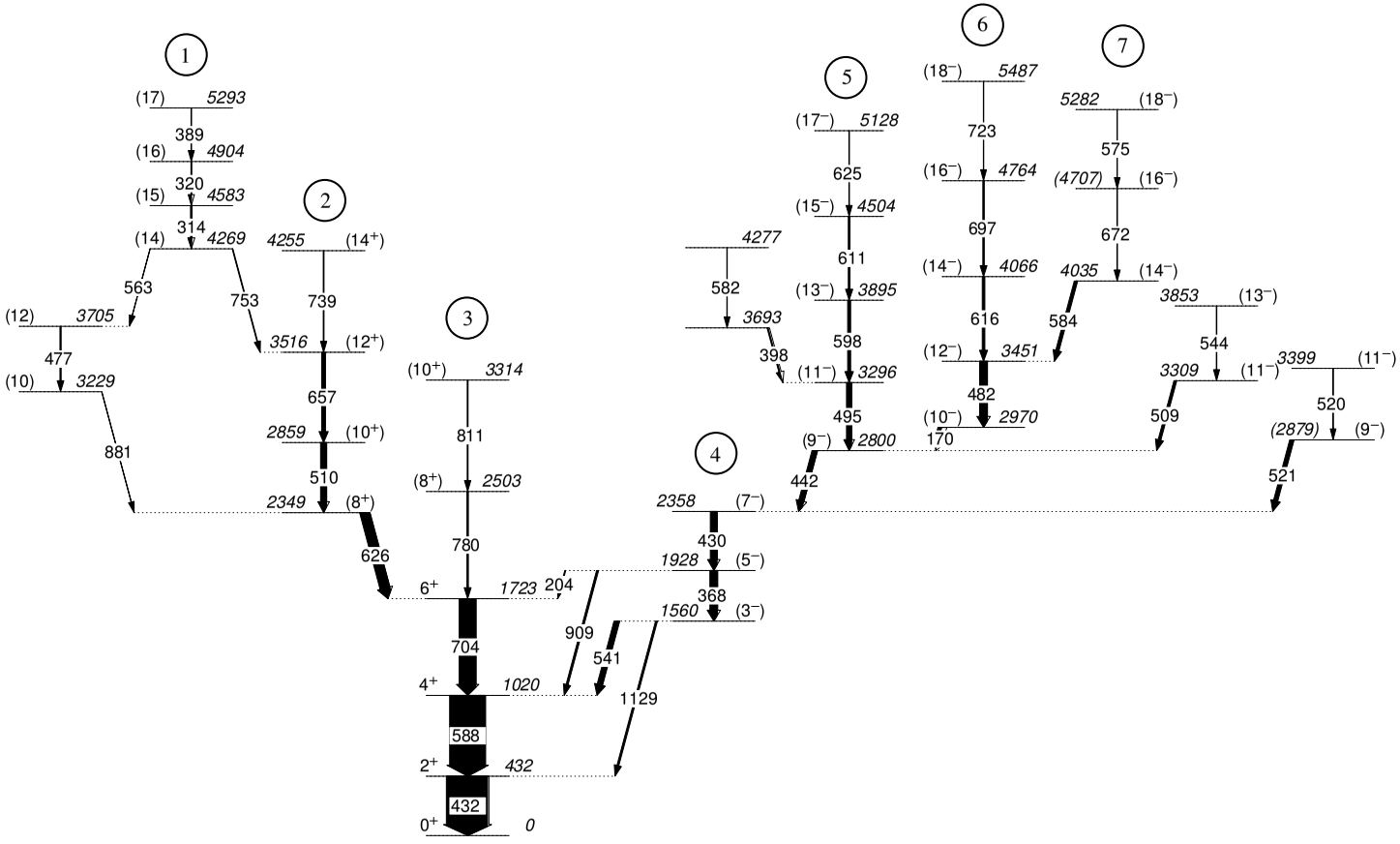

Figure 4.3. The level scheme of ^{166}Os established in the present work. The γ-ray energies are given in keV and the widths of the arrows correspond to the intensities of the γ-ray transitions. The levels are labeled with their spin and parity, and the excitation energies are given in keV with respect to the 0^+ ground state. Parenthesis indicate that the assignments are tentative.

Table 4.1. The energies and intensities of the observed γ rays. The intensities have been normalized with respect to the $2^+ \rightarrow 0^+$ transition. For transitions above the (9_1^-) state normalization is done with respect to the intensities of 442 keV and 170 keV γ rays, as the measured intensities below the (9_1^-) are too low due to the long lifetime of the (9_1^-) state.

E_γ (keV)	I_γ (%)	E_i (keV)	$I_\mathrm{i} \rightarrow I_\mathrm{f}$
169.6 (8)	9.1(1)	3020	$(10^-) \rightarrow (9^-)$
204.5(6)	2.1(2)	1928	$(5^-) \rightarrow (6^+)$
313.9(6)	3(3)	4583	$(15) \rightarrow (14)$
320.4(6)	1.5(2)	4904	$(16) \rightarrow (15)$
347.7(8)	2.6(4)	3693	
368.1(6)	18.2(8)	1928	$(5^-) \rightarrow (3^-)$
389.3(7)	1.2(2)	5293	$(17) \rightarrow (16)$
430.0(6)	16.5(8)	2358	$(7^-) \rightarrow (5^-)$
432.0(6)	100(5)	432	$2^+ \rightarrow 0^+$
442.4(6)	12.8(5)	2800	$(9^-) \rightarrow (7^-)$
476.5(6)	2.8(3)	3705	$(12) \rightarrow (10)$
481.9(8)	18.6(11)	3501	$(12^-) \rightarrow (10^-)$
495.3(8)	12.5(3)	3346	$(12^-) \rightarrow (9^-)$
509.1(12)	6.5(10)	3309	$(11^-) \rightarrow (9^-)$
510.4(6)	14.6(7)	2859	$(10^+) \rightarrow (8^+)$
520.3(12)	0.5(3)	3399	$(11^-) \rightarrow (9^-)$
520.7(12)	10.2(6)	2879	$(9^-) \rightarrow (7^-)$
540.6(6)	13.4(8)	1560	$(3^-) \rightarrow 4^+$
543.6(12)	1.2(4)	3853	$(13^-) \rightarrow (11^-)$
563.3(7)	0.8(2)	4269	$(14) \rightarrow (12)$
575.4(9)	0.5(3)	5332	$(18^-) \rightarrow (16^-)$
582.5(9)	0.9(3)	4277	
583.9(8)	7.9(6)	4085	$(14^-) \rightarrow (12^-)$
588.4(6)	86(4)	1020	$4^+ \rightarrow 2^+$
597.9(8)	7.1(5)	3944	$(13^-) \rightarrow (11^-)$
610.4(8)	4(4)	4554	$(15^-) \rightarrow (13^-)$
615.8(8)	6.2(5)	4116	$(14^-) \rightarrow (12^-)$
625.2(8)	1.3(3)	5178	$(17^-) \rightarrow (15^-)$
626.1(6)	24.2(10)	2349	$(8^+) \rightarrow (6^+)$
657.4(6)	9(4)	3516	$(12^+) \rightarrow (10^+)$
672.1(8)	1.3(3)	4757	$(16^-) \rightarrow (14^-)$
697.5(8)	3.4(4)	4814	$(16^-) \rightarrow (14^-)$
703.8(6)	41(2)	1723	$6^+ \rightarrow 4^+$
722.7(10)	0.8(3)	5537	$(18^-) \rightarrow (16^-)$
739.3(7)	1.8(3)	4255	$(14^+) \rightarrow (12^+)$
752.9(6)	1.8(2)	4269	$(14) \rightarrow (12^+)$
780.3(6)	3.4(4)	2503	$(8^+) \rightarrow 6^+$
811.1(7)	2(3)	3314	$(10^+) \rightarrow (8^+)$
880.5(7)	0.8(3)	3229	$(10) \rightarrow (8^+)$
909.3(6)	4.7(4)	1928	$(5^-) \rightarrow 4^+$
1128.5(6)	4.5(4)	1560	$(3^-) \rightarrow 2^+$

γ rays, it is clear that the feeding via the 780 keV γ-ray transition to the 6^+ state is fast compared to the other feeding. Therefore, the 780 keV and 811 keV transitions form the continuation of the ground-state band while the structure of the yrast sequence changes. In figure 4.4 d, the 314 keV γ-ray transition is used as a gate, revealing a sequence of low-energy transitions on top of the state at 4.3 MeV with decay path to the ground state from this state. Based on similar structures in other nuclei of this region, these transitions are suggested to form a cascade of dipole transitions (presumably M1) [Bark99, Peura14].

Figure 4.5 shows band 4 and the structures feeding it. In figure 4.5 a, the spectrum gated with the 368 keV γ rays shows 541 keV and 1129 keV transitions linking the negative-parity structures to the ground-state band. In figure 4.5 b the γ-ray spectrum in coincidence with the 442 keV γ rays assigned to depopulate the (9_1^-) state is shown. In figures 4.5 c and d, spectra showing bands 5-7 feeding the (9^-) state are presented. A clear difference in the relative intensities of the transitions feeding and depopulating the (9^-) state can be observed in figures b-d. This is caused by the long lifetime of the (9^-) state (see section 4.1.2). The detection efficiency of the γ rays emitted behind the target is low for detectors situated at forward angles and therefore, a large fraction of γ rays are not detected below the (9^-) state.

4.1.2 Lifetimes

In the RDDS measurement, data was collected with nine target-to-degrader distances ranging from $8 - 8000\,\mu$m. For the analysis, the characteristic α decay of ^{166}Os was required similarly as in the analysis of the excited states. The lifetime of the 2^+ state was analyzed from the $\gamma\gamma$-coincidence data and the lifetimes of the (8_1^+) and (9_1^-) states from the γ-ray singles data. Due to the long lifetime of the (8_1^+) state compared to the lifetimes of 4^+ and 6^+ states, it was not possible to obtain lifetimes for the 4^+ and 6^+ states.

In the analysis of the lifetime of the 2^+ state the 430 keV $(7^-) \rightarrow (5^-)$ γ ray (in figure 4.3 band 4) has to be taken into account. The γ-ray energies are too close to each other (430.0 keV for the $(7^-) \rightarrow (5^-)$ transition and 432.2 keV for the $4^+ \rightarrow 2^+$ transition) to enable reliable fitting at the same time for both components. In order to clean up most of the feeding from the negative-parity

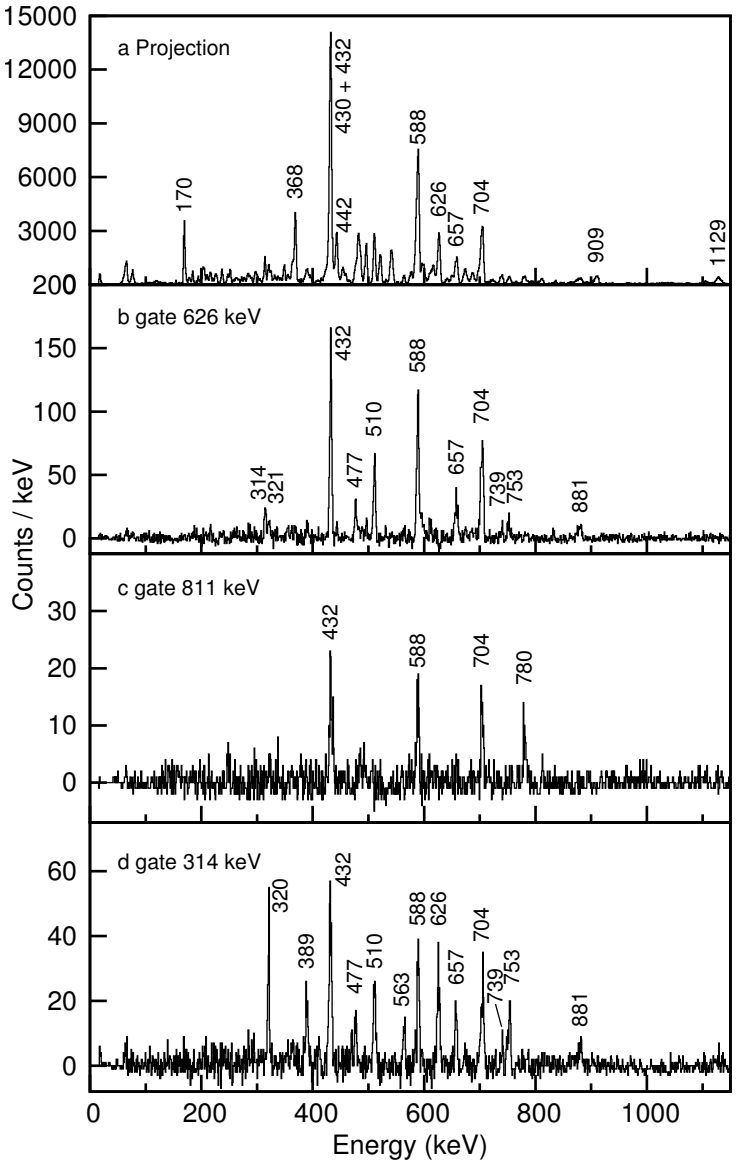

Figure 4.4. (a) Projection of the $\gamma\gamma$ matrix correlated with the ^{166}Os α decay, see the text for details. Also, the spectra (b)-(d) are similarly correlated. (b) γ rays in coincidence with the 626 keV transition showing the yrast structures. (c) γ rays in coincidence with the 811 keV transition illustrating the ground-state band (band 3 in figure 4.3). (d) γ rays in coincidence with the 314 keV transition showing bands 1-3.

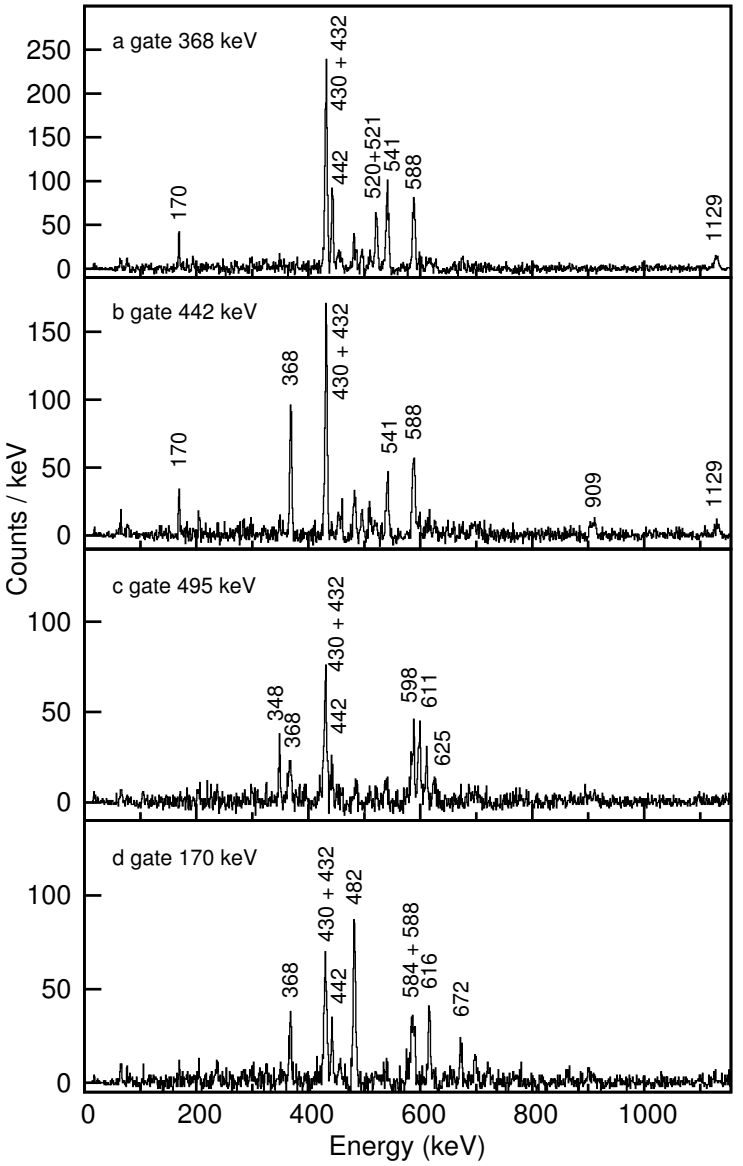

Figure 4.5. (a) Coincidence γ-ray spectra for the 368 keV γ ray. (b) Gamma rays in coincidence with the 442 keV transition. (c) A coincidence spectrum for the 495 keV transition showing band 5 feeding the (9_1^-) state. (d) Gamma rays in coincidence with the 170 keV γ ray showing bands 6 and 7 feeding the the (9^-) state. In all cases, correlation with the ^{166}Os α decay is required.

states and thus the intensity of the 430 keV transition, $\gamma\gamma$ coincidences were analyzed. A sum gate consisting of the 704 keV, 626 keV and 510 keV transitions was used. Both the feeding transition and the depopulating transition were fitted in these spectra. An example for the depopulating transition is shown in figure 4.6 a. The 625 keV $(17^-) \rightarrow (15^-)$ transition in band 5 and the 509 keV $(11_2^-) \rightarrow (9_1^-)$ transition feeding to band 4 were included to the gate due to similar energies as those transitions used for gating. Thus, some of the intensity of the 430 keV transition remains in the gated spectra. Some of the the feeding coming via the 430 keV transition goes directly to the 2^+ state via the 1129 keV $(3^-) \rightarrow 2^+$ transition. This side feeding has similar time behavior as the feeding proceeding via the 541 keV $(3^-) \rightarrow 4^+$ and 909 keV $(5^-) \rightarrow 4^+$ transitions as the lifetime of the 4^+ state is short compared to the lifetime of the (9_1^-) state. The intensity of the 430 keV γ-ray transition in the gated spectra was determined to be less than 7% of the intensity of the 432 keV transition from the areas of the 204, 540 and 910 keV γ-ray peaks. As the feeding via the negative-parity band is slow, the doublet does not have a distinguishable effect on the lifetime of the 2^+ state.

The lifetime of the yrast 8^+ state was analyzed from γ-ray singles spectra. The spectra were sorted separately for every distance and every Jurogam II ring. In order to obtain more spectra at different angles, no add-back was used for γ rays scattering between clover crystals with different angle to the beam axis. With this, also the $\theta = 71°$ and $\theta = 109°$ crystals of the clovers were suitable for the analysis. Therefore, the lifetime was calculated as an average from the individual values obtained for four different angles. As the intensity of the feeding 881 keV γ ray transition is low, fitting of the components was not possible. Instead, it was assumed to have similar time behavior to that of the 510 keV γ-ray transition. Also the 625 keV and the 509 keV transitions are included in the γ-ray peaks. Fitting the two components of the 495 keV γ ray below the 625 keV γ ray indicates that the 625 keV transition must be fast. As the intensity of the shifted component of the 626 keV is small for the short distances, it is clear that the doublet does not have an effect on the decay curve. It is not possible to obtain a lifetime for the 10_1^+ state due to the 509 keV transition, but a rough estimate of $\tau < 10$ ps can be obtained from the decay curve of the 510 keV transition. As this estimate is an order of magnitude shorter than the lifetime of the 8_1^+ state, the doublet of the feeding state does

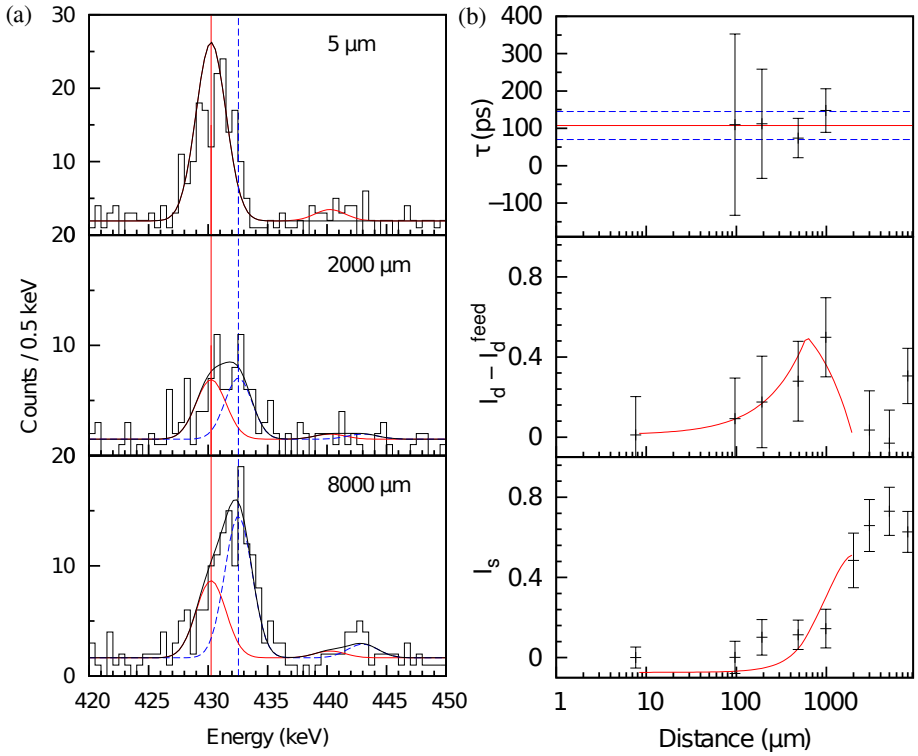

Figure 4.6. (a) The fitted γ-ray peaks for the 432 keV $2^+ \rightarrow 0^+$ transition detected at $\theta = 71°$ are shown. Also the 442 keV γ-ray peak is fitted to give an indication of the strength of the 430.0 keV $(7^-) \rightarrow (5^-)$ γ-ray transition. (b) The shifted component and the difference of the degraded components of the depopulating and feeding transition are shown as a function of the target-to-degrader distance. All of the intensities have been normalized by the total intensity of the γ-ray transition. The values of the lifetime are extracted within the region of sensitivity together with the average.

Table 4.2. The measured lifetimes for the excited states in ^{166}Os and the corresponding $B(E2)$ values. The lifetimes of the 2^+ and 8_1^+ states were analyzed from the RDDS data and the lifetime for the (9_1^-) state was obtained using the RSAM method.

Level	τ (ps)	E_γ (keV)	B(E2)(e^2b^2)	B(E2)($W.u.$)
2^+	130(30)	432.2	0.042(10)	7(2)
8^+	110(40)	625.7	0.008(3)	1.4(5)
(9^-)	1100(200)	442.4	0.0042(8)	0.77(15)

not have an effect on the lifetime of the 8_1^+ state.

As the measured distances were not long enough to cover the region of sensitivity for the (9_1^-) state, only a rough estimate of $0.5-2$ ns for its lifetime was obtained from the RDDS data. For a more precise result, an RSAM analysis was employed. Alpha-decay correlated γ-rays detected in the clover detectors were used in the analysis. As the method is based on the observed asymmetry in the clover crystals, only the γ rays scattering in the same crystal ring were accepted for the add-back and others were discarded from the analysis. Only the data measured at the shortest target-to-degrader distance 8 µm were included in the analysis, as otherwise corrections would be needed for the target position and recoil-velocity distribution.

The measured γ-ray spectra at $\theta = 71°$ and at $\theta = 109°$ are shown in figure 4.7 a and b. While the areas of the 170 keV and 704 keV γ ray peaks are almost same at both angles there is a strong suppression of the intensities of γ-ray transitions below the (9_1^-) state for $\theta = 109°$. The asymmetries A_γ were determined for 170 keV and 442 keV transitions according to equation 3.3. The intensities were fitted separately for all of the clover rings and the areas were normalized with the efficiency of the detector ring. The asymmetry spectrum is shown in figure 4.7 c. The obtained value for $A_\gamma(170\,\text{keV}) = 0.009(2)$ confirms the symmetry for fast transitions. For the 442 keV γ ray, $A_\gamma(442\,\text{keV}) = 0.15(4)$.

The efficiency of the clover crystals as a function of the distance behind the target was simulated with the GEANT4 simulation tooolkit [Agostinelli03] by D. Cox [Cox17]. The results are shown in figure 4.8. The simulations were run with realistic detector geometries. Already 2 cm behind the target position the efficiency of the crystals at forward angles ($\theta = 109°$) has decreased to 71%

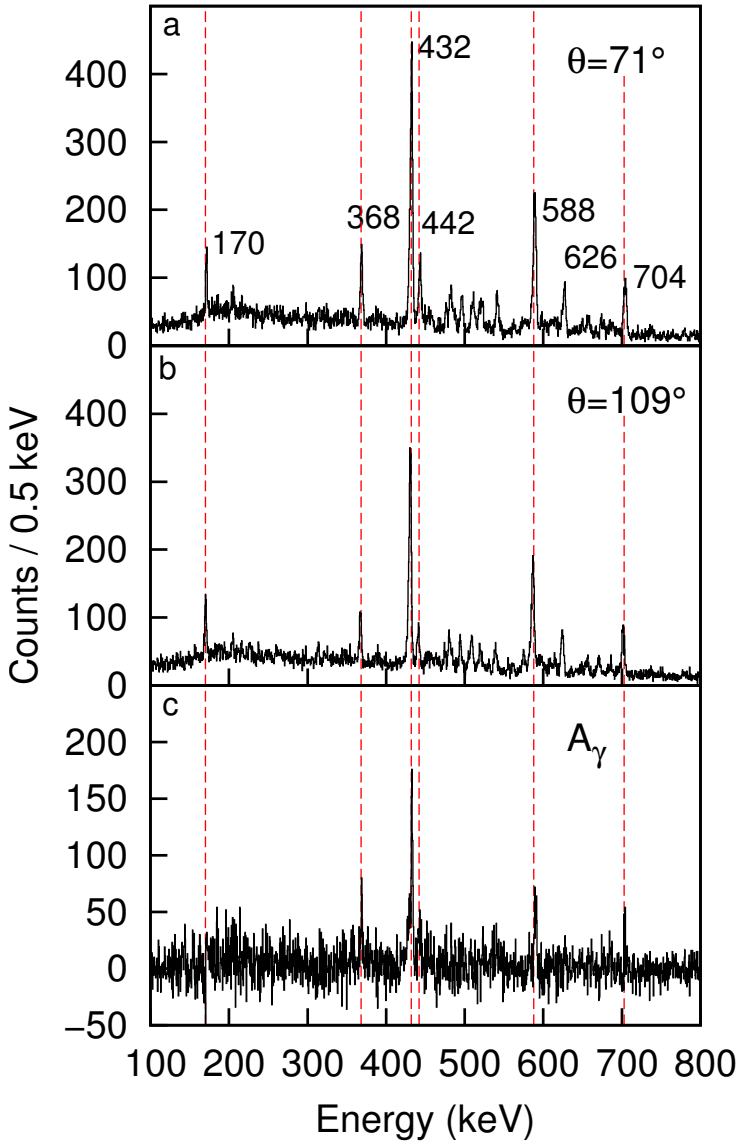

Figure 4.7. (a) The γ-ray spectrum for the clover crystals at $\theta = 71^\circ$ correlated with the ^{166}Os α decay. b) The γ-ray spectrum for $\theta = 109^\circ$. c) The measured asymmetry $I_\gamma(\theta = 71^\circ) + I_\gamma(\theta = 100^\circ) - I_\gamma(\theta = 80^\circ) - I_\gamma(\theta = 109^\circ)$.

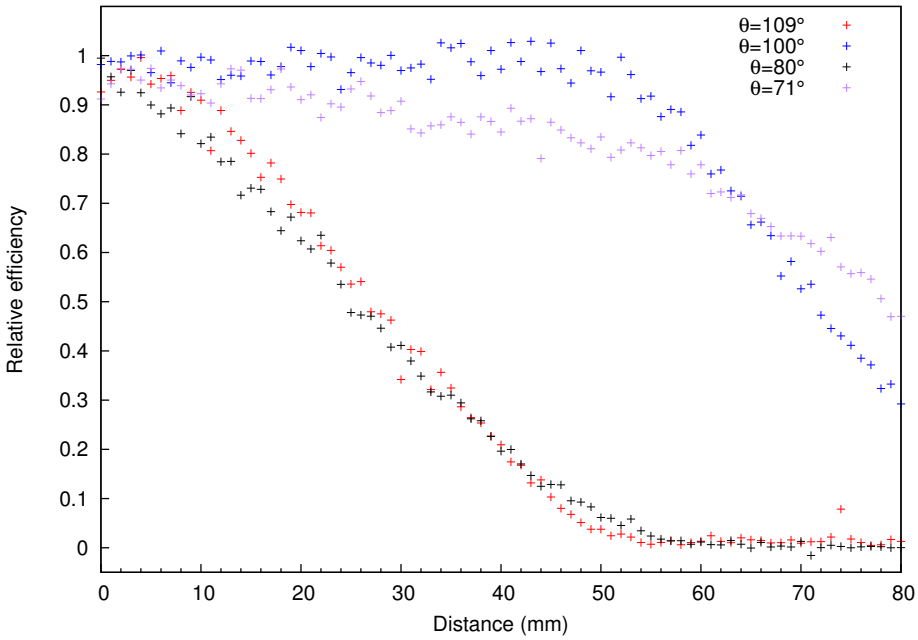

Figure 4.8. The efficiency of the clover crystals as a function of γ ray emission at different distances behind the target. The simulations were run with the GEANT4 toolkit with realistic detector geometries.

while the efficiency of the detectors at backward angles ($\theta = 71°$) is still of 99% the efficiency at the target position.

A set of polynomials were used to fit the total efficiency ϵ_0 and the asymmetry in the efficiencies $\Delta\epsilon$. The integral in equation 3.6 was numerically calculated for $v\tau$ values. The resulting curve is shown in figure 4.9 together with the determined $v\tau(9^-)$ value.

4.2 ^{168}Os

A total of 9.3×10^6 recoil-gated $\gamma\gamma\gamma$ coincidences were detected in two experiments dedicated to study the excited states of ^{168}Os. The used reaction, beam energy and set-up are effectively the same as in the RDDS measurement, see table 3.1. The analysis was performed with these three-fold coincidences and

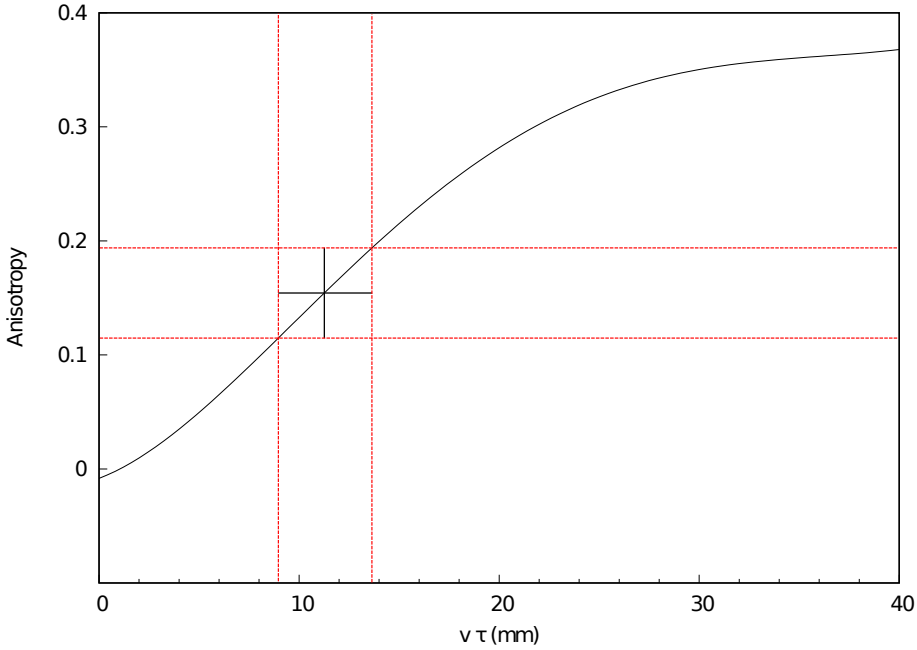

Figure 4.9. The calculated anisotropy as a function of $v\tau$. The measured anisotropy for the 442 keV γ-ray transition is marked, and the resulting value for $v\tau$.

the resulting level scheme is presented in figure 4.10. However, in the present work the focus is on the lifetime measurements.

4.2.1 Lifetimes

The experimental details of the RDDS measurement of the lifetimes of ^{168}Os are summarized in table 3.1. As the α-decay branching ratio is lower than in ^{166}Os and the half-life is longer, only recoil gating was used in the analysis of $\gamma\gamma$ coincidences. The higher production cross section with gating provides clean enough spectra for lifetime analysis. In the analysis of singles γ-ray spectra, characteristic α decay was required to help clean the spectra.

In the experiment, data were collected for thirteen target-to-degrader distances, ranging from $5 - 8000\,\mu$m. Due to a break in the experiment, the beam had to be tuned again. Also the target and the degrader were changed at this point. In the first part of the experiment the recoil velocity after the target was $v_1/c = 0.034$ and in the second part $v_2/c = 0.040$. It was possible to align all of the shifted components with the Doppler corrections but not the degraded components. For the 341 keV γ ray the difference in the positions of the degraded components was 0.5 keV when the shifted components were aligned.

The distances measured in the first and second part of the experiment are summarized in table 4.3. Combining these two sets of distances is difficult due to the inaccuracy in the determination of the absolute distances. In principle $1000\,\mu$m, which was measured twice, could be used for determining the difference in the absolute distances from the measured intensity ratios $I^{\mathrm{u}}/I^{\mathrm{s}}$. Due to different recoil velocities and the length of the distance, the precision is not comparable to the precision of relative distances. The longer distances can be combined as the relative error of the distances remains small. The lifetimes, for which the the region of sensitivity was at shorter distances than $100\,\mu$m, were analyzed separately for both set of distances.

Lifetimes of the 2^+ and the 4^+ states were determined from the $\gamma\gamma$ coincidences. For the (12^+), (14^+), (5^-) and (7^-) states, statistics were not sufficient to

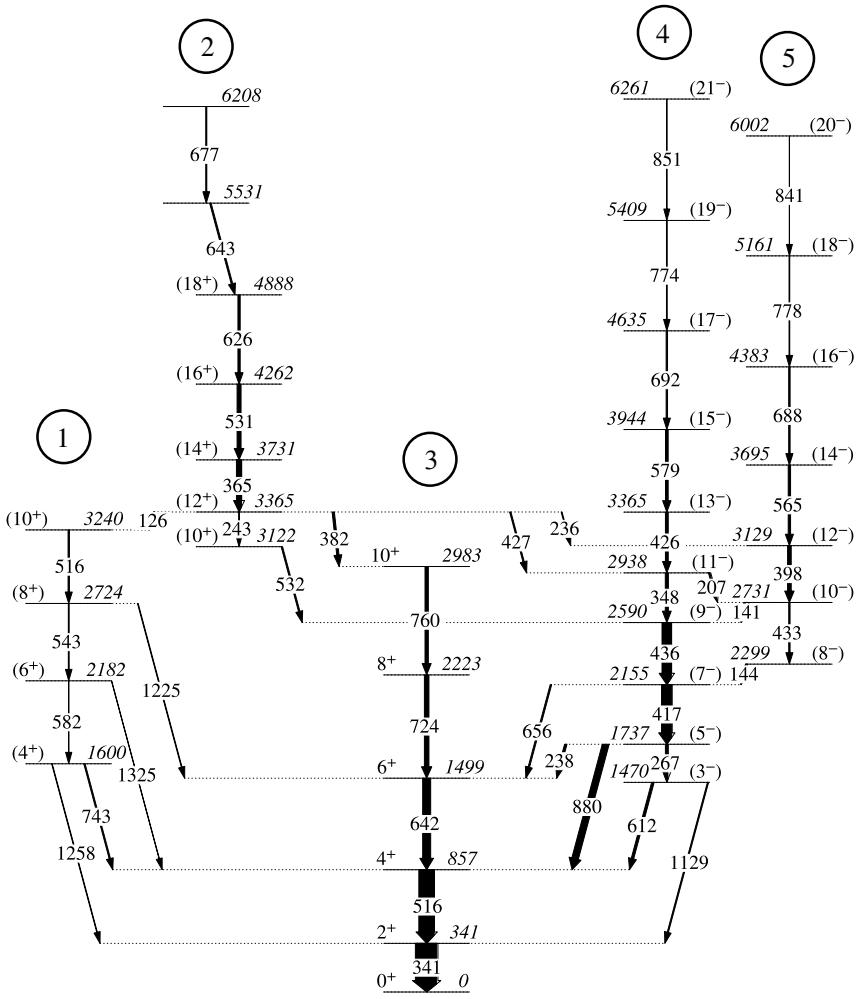

Figure 4.10. The level scheme for ^{168}Os.

Table 4.3. The RDDS measurement of ^{168}Os was conducted in two parts. Both sets of the distances have their own calibration. The data were measured for target-to-degrader distance 1000 µm in both sets. The distances are given in µm.

Set I	Set II
5	21
100	40
500	70
1000	250
1800	1000
3200	2300
8000	5000

enable coincidence analysis. Only in the first two rings of Jurogam I, the γ-ray energies of the shifted and degraded components were sufficiently separated.

Both the $4^+ \rightarrow 2^+$ and the $6^+ \rightarrow 4^+$ transitions are self-coincident doublets. The 516.3 keV, $4^+ \rightarrow 2^+$ transition is a doublet with the 515.5 keV $(10^+) \rightarrow (8^+)$ transition in band 1. Also the 642 keV, $6^+ \rightarrow 4^+$ transition is a doublet with the 643 keV transition to the (18^+) state in band 2.

Feeding of the 4^+ state via the 880 keV transition is too slow compared to the lifetime of the 4^+ state to enable any lifetime analysis. Thus the 642 keV γ ray had to be used as the feeding transition. The analysis was done by gating with both components of the feeding transition. The time distribution of the feeding transition was obtained by gating with the depopulating transition. The gate on the 642 keV γ ray also included the 643 keV γ rays. This causes side feeding via other transitions feeding the 4^+ state. It also changes the feeding time distribution.

The intensity of the side feeding can be approximated by comparing the intensities of the 643 keV γ ray and the 642 keV γ rays. They are in ratio $I(643)/I(642) = 0.18$. The 643 keV transition feeds the (18^+) state depopulated by the 626 keV transition (65% of the total intensity of the 626 keV γ ray). Fitting the components of the 626 keV γ ray gives only the shifted component in the summed spectrum of all distances. This indicates that also the 643 keV γ-ray transition has to be fast. Since in equation 3.12 only the degraded component of the feeding transition is used, the 643 keV γ-ray transition does not cause

any error, if external normalization for the intensities is used. For this, the transition intensities of the yrast band up to spin 12^+ in coincidence with the $2^+ \rightarrow 0^+$ transition were used for normalization as to check the result obtained by using normalization with total intensities. No difference was found in the decay curves and the resulting lifetimes for the 4^+ state. The relative intensity of the 515.5 keV transition is 8.6% of the intensity of the 516.3 keV $4^+ \rightarrow 2^+$ transition and therefore the effect it may have on the lifetimes of the 2^+ and the 4^+ states is smaller than the statistical uncertainty.

For the analysis of the other states the feeding via the transitions visible in figure 4.10 were taken into account. The unobserved feeding was assumed to have a similar time behavior as the feeding via the states marked in the level scheme in figure 4.10. The uncertainty in the feeding is smaller than the statistical uncertainty.

An example of the peaks for the $2^+ \rightarrow 0^+$ and $4^+ \rightarrow 2^+$ transitions is shown in figures 4.11 and 4.12. The extracted lifetimes and the corresponding decay curves are also presented. All of the measured lifetimes and the corresponding $B(E2)$ and $B(E1)$ values are summarized in table 4.4. The internal conversion coefficients are form [Kibédi08]. Also the transition quadrupole moments have been deduced for the $E2$ transitions.

Table 4.4. The measured lifetimes for the excited states in ^{168}Os and the coresponding $B(E1)$ and $B(E2)$ values for the depopulating transitions. Quadrupole moments have been calculated for the $E2$ transitions.

I^π	τ (ps)	$I_\mathrm{i}^\pi \to I_\mathrm{f}^\pi$	E_γ (keV)	$B(E2)$ ($e^2\mathrm{b}^2$)	$B(E2)$ (W.u.)	$\lvert Q_\mathrm{t}\rvert$ (eb)	$B(E1)$ (10^{-3}W.u.)
2^+	41(7)	$2^+ \to 0^+$	341.1	0.41(7)	74(13)	4.5(4)	
4^+	16(8)	$4^+ \to 2^+$	516.3	0.14(7)	25(13)	2.2(6)	
(12^+)	740(50)	$(12^+) \to 10^+$	382.3	0.0048(4)	0.86(6)	0.37(3)	
		$(12^+) \to (10^+)$	125.8	0.24(2)	43(3)	2.6(2)	
		$(12^+) \to (10^+)$	243.3	0.0105(7)	1.90(13)	0.55(4)	
		$(12^+) \to (12^-)$	236.1				0.0068(5)
		$(12^+) \to (10^-)$	426.8				0.00074(5)
(14^+)	17(2)	$(14^+) \to (12^+)$	365.4	0.70(9)	130(15)	4.5(3)	
(5^-)	59(7)	$(5^-) \to (3^-)$	267.0	0.22(3)	40(5)	3.2(4)	
		$(5^-) \to 4^+$	879.9				0.0045(6)
		$(5^-) \to 6^+$	237.6				0.076(9)
(7^-)	21(4)	$(7^-) \to (5^-)$	417.3	0.26(3)	48(5)	4.2(4)	
		$(7^-) \to 6^+$	656.3				0.0064(7)

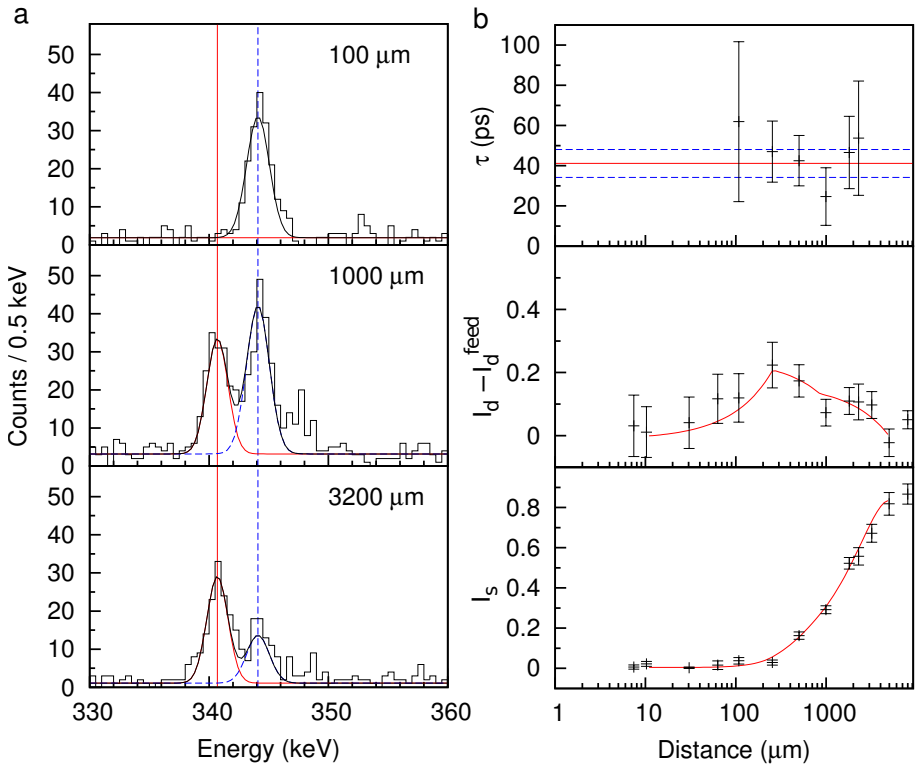

Figure 4.11. a) The fitted peaks for $2^+ \rightarrow 0^+$ transition in ^{168}Os gated by the feeding 516 keV γ ray for 100, 1000 and 3200 µm. b) The individual values for the lifetime for the distances within the region of sensitivity. All of the intensities have been normalized by the total intensity of the γ-ray transition. Also the fits of the degraded and shifted components are shown.

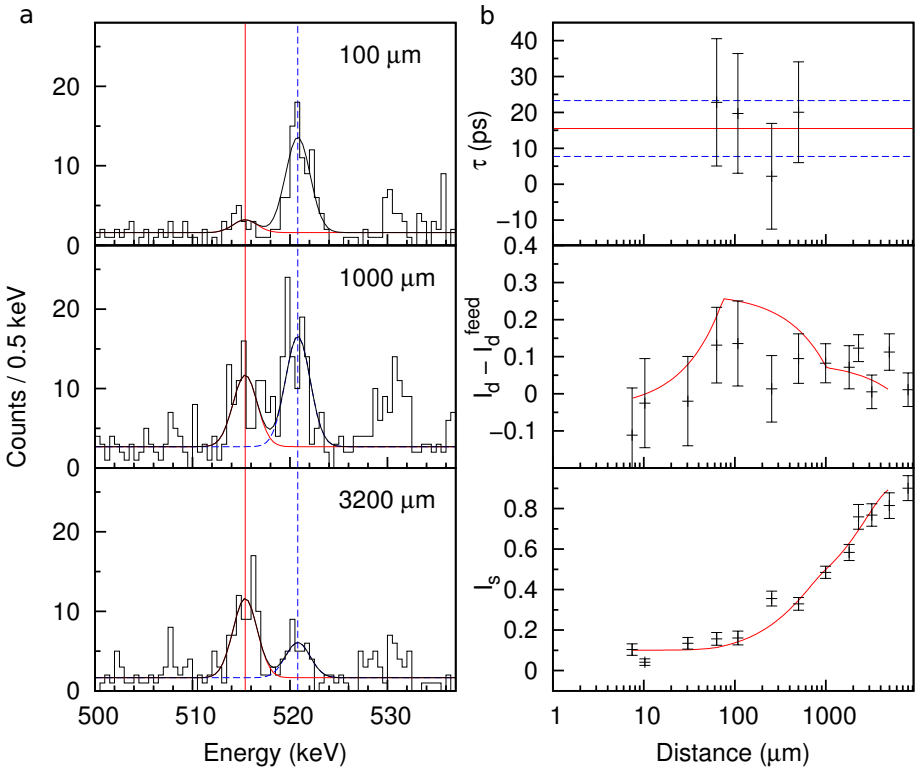

Figure 4.12. a) The fitted peaks for $4^+ \rightarrow 2^+$ transition in ^{168}Os gated by the feeding 642 keV γ ray for 100, 1000 and 3200 µm. b) The individual values for lifetime for the distances within the region of sensitivity. All of the intensities have been normalized by the total intensity of the γ-ray transition. Also the fits of the degraded and shifted components are shown.

Chapter 5

Discussion

The excitation energies of the first excited states in the yrast sequence are shown for even-even osmium isotopes in figure 5.1. Also the energies of the second 8^+ and 10^+ states are included for $^{162-170}$Os. At the neutron mid-shell the excitation energies of the first 2^+ and 4^+ states are almost constant. This is a good indication of the deformed structures becoming yrast at mid-shell similarly to the platinum isotopes [Lee88, Le Blanc99]. The measured transition probabilities of the lowest transitions in $^{176-180}$Os confirm the collective structures [Möller05]. When moving to more neutron-rich nuclei the excitation energies increase gradually; the axially symmetric prolate rotors at mid-shell evolve to oblate structures and γ softness or vibrational excitations near the $N = 126$ closed shell [John14, Podolyák09].

For the neutron-deficient isotopes, there is a drastic change in the structure of the first excited states at $A < 174$. The increasing excitation energies indicate a decrease in collectivity. The level energies suggest shape coexistence in ^{172}Os [Davidson94] and this has been confirmed with the lifetime measurements [Virtanen95]. For the lighter osmium isotopes the energy of the deformed band head is expected to increase. In ^{168}Os cranked shell model calculations place the band head at 1.9 MeV [Joss01]. The ratio of the excitation energies of the first states, $E(4^+)/E(2^+)$, indicates that the more neutron-deficient nuclei are triaxial and ^{162}Os is observed to be vibrational [Joss04].

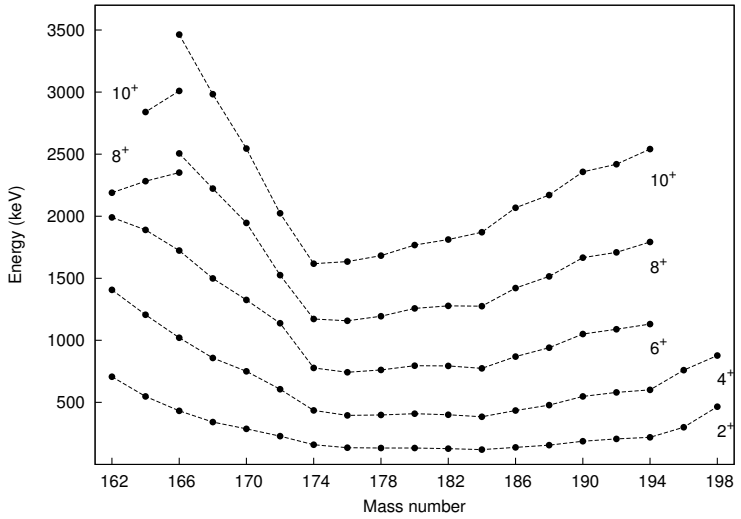

Figure 5.1. The excitation energies of the first excited states of the yrast states for the even-even osmium isotopes. For $^{162-168}$Os the second 8^+ and 10^+ states have been also plotted. Data taken from [Joss04, King00, Dracoulis88, Davidson94, Browne99, Basunia06, Achterberg09, Mccutchan15, Singh15, Baglin10, Baglin03, Singh02, Singh03, Baglin12, Daniel17, John14, Podolyák09].

It is clear from the excitation energies of the 8^+ and 10^+ states that the structure of the yrast sequance changes at spin 8^+ when moving from ^{168}Os to ^{166}Os. A similar change occurs between ^{162}W and ^{164}W [Joss16]. This change in the structure in the osmium isotopes is supported by the (8_2^+) and (10_2^+) states discovered in the present study. Furthermore, the reduced transition probability $B(E2; 8_1^+ \rightarrow 6^+) = 1.4(5)$ W.u. in 166Os confirms the poor overlap of the wave functions of these states. The lifetime of the (8_2^+) state can be deduced to be short compared to the lifetime of the 8_1^+ state from the decay curve of the 6^+ state, but the feeding is too weak to enable any quantitative measurement.

Band 1 in figure 4.3 resembles the dipole bands found in ^{171}Ir [Bark99] and ^{173}Pt [Peura14]. The γ-ray intensities were too weak to determine the type of the transitions the from angular distributions. Electric quadrupole transitions with such low transition energies would require superdeformation or a high K quantum number (angular momentum projection to the symmetry axis) for the band. Superdeformation is not very likely. Also, if the band were a high-K state, it would be isomeric. From the decay curve of the 510 keV transition, it is clear that the (14) state at 4.3 MeV has a short lifetime. Therefore, the transitions were marked as dipole.

The lowest transitions in the negative-parity band (band 4 in figure 4.3) and the connecting transitions to the ground-state band in ^{166}Os resemble those in ^{168}Os, ^{170}Os [Dracoulis88] and ^{172}Pt [Joss05]. The spin and parity assignments are tentative as the long lifetime of the (9^-) distorts the angular distributions of the γ rays. The low reduced transition probability $B(E2; (9^-) \rightarrow (7^-)) = 0.77(15)$ W.u indicates a change in the structure. Therefore, the (9_1^-) state has been marked to belong to band 5. There is a change in the structure also in ^{168}Os in bands 4 and 5 as the feeding of the 4^+ state is considerably slower via these bands than the ground-state band even though the majority of this feeding comes via the 12^- state. In ^{162}W and ^{164}W there are low-energy γ-ray transitions in the negative parity structures [Joss16] indicating a change in the structure as well.

The reduced transition probabilities of the $2^+ \rightarrow 0^+$ and $4^+ \rightarrow 2^+$ transitions are shown on figure 5.2 together with the ratio $B(E2)_{4/2} = B(E2; 4^+ \rightarrow 2^+)/B(E2; 2^+ \rightarrow 0^+)$. On the neutron-rich side of the mid-shell, the $B(E2; 2^+ \rightarrow 0^+)$ and $B(E2; 4^+ \rightarrow 2^+)$ decrease smoothly with the $4^+ \rightarrow 2^+$ transition stay-

ing more collective than the $2^+ \rightarrow 0^+$ transition. On the neutron-deficient side of the mid-shell the decrease of collectivity is faster and more drastic than expected. While the $2^+ \rightarrow 0^+$ transition is still collective in ^{168}Os ($B(E2) = 74(13)$ W.u.), in ^{166}Os the transition probability $B(E2) = 7(2)$ W.u. resembles those of single-particle excitations at closed shells. A similar drop in collectivity has been measured between ^{164}W and ^{162}W, where the reduced transition probability drops from 150(100) W.u to 31(13) W.u.

While the $2^+ \rightarrow 0^+$ transition is collective in ^{168}Os, the $4^+ \rightarrow 2^+$ transition is no longer as collective with $B(E2; 4^+ \rightarrow 2^+) = 27(9)$ W.u.. All of the collective models predict the ratio $B(E2)_{4/2} = B(E2; 4^+ \rightarrow 2^+)/B(E2; 2^+ \rightarrow 0^+)$ to be larger than unity. Classical exceptions to this are shape-coexisting structures near closed shells and seniority structures. If the ground state and the first excited 2^+ state belong to a different collective structure than the 4_1^+ state, $B(E2)_{4/2} < 1$ is theoretically possible, however it has never been observed. For instance in mercury isotopes, the higher lying transition is always more collective and the $B(E2)_{4/2} > 1$ for the first transitions [Bree14b]. The osmium isotopes under study are situated not near closed shells and thus shape-coexistence is not expected [Joss01].

A recent study of ^{166}W has revealed similar transition probabilities as in ^{168}Os [Saygi17]. The $2^+ \rightarrow 0^+$ transition in ^{166}W is collective with $B(E2; 2^+ \rightarrow 0^+) = 150(9)$ W.u but the the next transitions in the yrast band with $B(E2; 4^+ \rightarrow 2^+) = 50(7)$ W.u and $B(E2; 6^+ \rightarrow 4^+) = 18(4)$ W.u are considerably less collective. It is interesting to note that also the $6^+ \rightarrow 4^+$ transition is not as collective as the $2^+ \rightarrow 0^+$ transition. This would be hard to explain in the framework of shape coexistence. Such a non-collective structure above a deformed structure would have larger level spacing and thus it would never reach the yrast line. With fusion-evaporation reactions such states would never be discovered.

In ^{166}Os the neutrons are expected to occupy the $\nu h_{9/2}$ orbitals and the almost full sub-shell could cause the measured low $B(E2; 8^+ \rightarrow 6^+)$ value, if the transition would be a seniority conserving transition. In ^{168}Os, the seniority scenario could explain the $B(E2)_{4/2} = 0.37(15)$ value as well as the reduced transition probabilities in ^{166}W. On the other hand, the first transition in ^{168}Os is too collective to be explained by seniority, which is a model for nuclei near

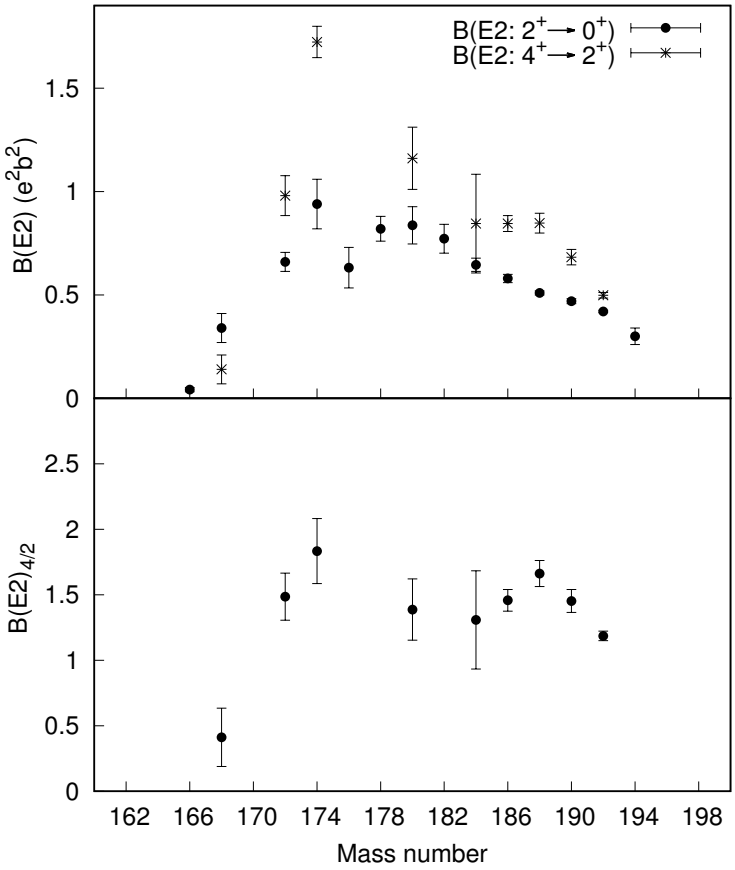

Figure 5.2. a) The reduced transition probabilities for the $2^+ \rightarrow 0^+$ and $4^+ \rightarrow 2^+$ transitions in even-even osmium isotopes. Data taken from [Virtanen95, Gascon87, Möller05, Pritychenko16, Milner71, Daniel17]. b) The ratio $B(E2)_{4/2} = B(E2; 4^+ \rightarrow 2^+)/B(E2; 2^+ \rightarrow 0^+)$.

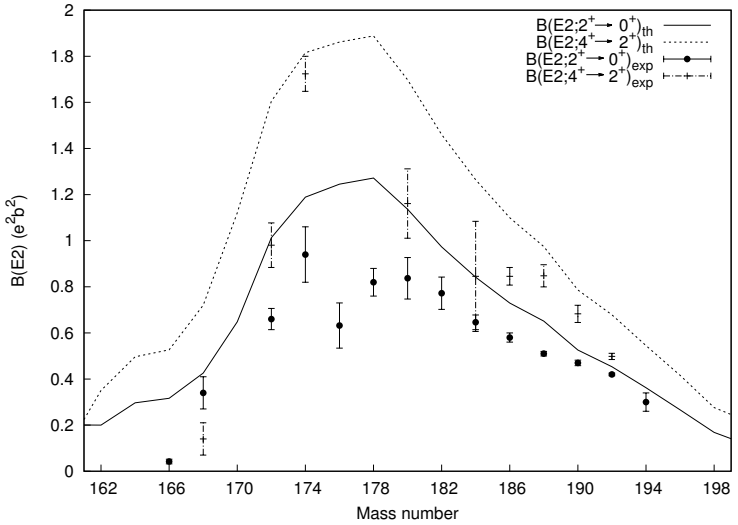

Figure 5.3. Theoretical results for the reduced transition probabilities $B(E2; 2^+ \rightarrow 0^+)$ and $B(E2; 4^+ \rightarrow 2^+)$ from the Hartree-Fock-Bogoliubov theory using the Cogny D1S effective nucleon-nucleon interaction [Delaroche10]. Experimental data is shown, taken for heavier isotopes from [Virtanen95, Gascon87, Möller05, Pritychenko16, Milner71, Daniel17].

closed shells with transition probabilities of a few W.u.

Delaroche et al. have carried out global calculations of several spectroscopic properties of even-even nuclei using the Hartree-Fock-Bogoliubov theory using the Cogny D1S effective nucleon-nucleon interaction [Delaroche10]. The calculated $B(E2; 2^+ \rightarrow 0^+)$ and $B(E2; 4^+ \rightarrow 2^+)$ values are shown in figure 5.3 together with the experimental data. While the model reproduces the general trend of the $B(E2)$ values as expected, it fails to reproduce the measured low values for $B(E2; 2^+ \rightarrow 0^+)$ in ^{166}Os and $B(E2; 4^+ \rightarrow 2^+)$ in ^{168}Os. It is possible that the γ soft triaxial shape of these nuclei is the explanation for the measured $B(E2)$ values, but further theoretical calculations would be needed.

Chapter 6

Summary and Outlook

The level scheme for ^{166}Os has been expanded with the use of $\gamma\gamma$-coincidences correlated with the characteristic α decay. A change in the structure of the yrast band at spin 8^+ has been confirmed by the low transition probability, $B(E2; 8^+ \rightarrow 6^+) = 1.4(5)$ W.u.. Two new γ-ray transitions have been discovered to continue the ground-state band. A dipole band has been discovered at 4.3 MeV. The negative parity structures have been extended and three new bands are placed to feed the negative-parity band via an isomeric (9^-_1) state.

Lifetimes of the excited states in ^{166,168}Os have been measured with the Recoil Distance Doppler-Shift measurements. The lifetime of the 2^+ state in ^{166}Os was measured from $\gamma\gamma$ coincidences correlated with the α decay. For the (8^+_1) state α-decay correlated γ rays were analyzed and the lifetime of the (9^-) state was obtained with the Recoil Shadow Anisotropy method, as the measured distances were not long enough to cover the region of sensitivity. For 2^+ and 4^+ states in ^{168}Os, recoil-correlated $\gamma\gamma$ coincidences were analyzed and the rest of the lifetimes were obtained from α-decay correlated γ-ray spectra.

The reduced transition probabilities reveal a sudden decrease of collectivity of the $2^+ \rightarrow 0^+$ transition when moving from ^{168}Os to ^{166}Os. In ^{168}Os the first transition is still collective with $B(E2; 2^+ \rightarrow 0^+) = 74(13)$ W.u., while $B(E2; 2^+ \rightarrow 0^+) = 7(2)$ W.u. for ^{166}Os. Such low transition probabilities are expected only at shell closures with single-particle excitations.

The $4^+ \rightarrow 2^+$ transition in ^{168}Os is measured to be less collective than the $2^+ \rightarrow 0^+$ transition with $B(E2; 4^+ \rightarrow 2^+) = 27(9)$ W.u.. The ratio of the reduced transition probabilities is $B(E2)_{4/2} = 0.36(14)$. All of the collective models predict values larger than unity for the $B(E2)$ ratio. A similar $B(E2)_{4/2}$ value has been recently measured in ^{166}W [Saygi17]. An alternative method to measure the reduced transition probability for the $4^+ \rightarrow 2^+$ transition in ^{166}Os would be with Coulomb excitation. Due to small production cross sections for highly neutron-deficient osmium isotopes in the spallation of uranium, it is at present not possible.

Modern nuclear models fail to reproduce the measured transition probabilities. The γ softness and triaxial shapes may have an effect on the reduced transition probabilities but more measurements are needed to draw any final conclusions. An RDDS measurement has already been run for ^{168}W and ^{170}Os at Gammasphere, Argonne and the analysis of the lifetimes is still in progress.

Bibliography

[Achterberg09] E. Achterberg *et al.* Nucl. Data Sheets **110**, 1473 (2009).

[Agostinelli03] S. Agostinelli *et al.* Nuclear Instruments and Methods in Physics Research Section A: Accelerators, Spectrometers, Detectors and Associated Equipment **506**, 250 (2003).

[Alder75] K. Alder *et al.* Electromagnetic Excitation, Theory of Coulomb Excitatinon With Heavy Ions. North Holland Publishing Company (1975).

[Alexander65] T. K. Alexander *et al.* Canadian Journal of Physics **43** (1965).

[Alvarez93] C. R. Alvarez. Nucl. Phys. News **3** (1993).

[Appelbe02] D. E. Appelbe *et al.* Phys. Rev. C **66**, 014309 (2002).

[Baglin03] C. M. Baglin. Nucl. Data Sheets **99**, 1 (2003).

[Baglin08] C. M. Baglin. Nucl. Data Sheets **109**, 1103 (2008).

[Baglin10] C. M. Baglin. Nucl. Data Sheets **111**, 275 (2010).

[Baglin12] C. M. Baglin. Nucl. Data Sheets **113**, 1871 (2012).

[Banu05] A. Banu *et al.* Phys. Rev. C **72**, 061305 (2005).

[Bark99] R. A. Bark *et al.* Nuclear Physics A **A 657**, 113 (1999).

[Basunia06] M. Basunia. Nucl. Data Sheets **107**, 791 (2006).

[Beausang92] C. W. Beausang *et al.* Nuclear Instruments and Methods in Physics Research Section A: Accelerators, Spectrometers, Detectors and Associated Equipment **313**, 37 (1992).

[Bohr40] N. Bohr. Phys. Rev. **58**, 654 (1940).

[Bohr98] A. Bohr *et al.* Nuclear Structure. World Scientific (1998).

[Branford73] D. Branford *et al.* Nuclear Instruments and Methods **106**, 437 (1973).

[Bree14a] N. Bree *et al.* Phys. Rev. Lett. **112**, 162701 (2014).

[Bree14b] N. Bree *et al.* Phys. Rev. Lett. **112**, 162701 (2014).

[Brenn77] R. Brenn *et al.* Zeitschrift für Physik A Atoms and Nuclei **281**, 219 (1977).

[Browne99] E. Browne *et al.* Nucl. Data Sheets **87**, 15 (1999).

[Bucher16] B. Bucher *et al.* Phys. Rev. Lett. **116**, 112503 (2016).

[Carroll14] R. J. Carroll *et al.* Phys. Rev. Lett. **112**, 092501 (2014).

[Cederkäll07] J. Cederkäll *et al.* Phys. Rev. Lett. **98**, 172501 (2007).

[Cleemann78] L. Cleemann *et al.* Nuclear Instruments and Methods **156**, 477 (1978).

[Cox17] D. Cox. personal communication (2017).

[Cullen98] D. Cullen *et al.* Physical Review C **58**, 846 (1998).

[Daniel17] T. Daniel *et al.* Phys. Rev. C **95**, 024328 (2017).

[Davidson94] P. Davidson *et al.* Nuclear Physics A **568**, 90 (1994).

[Delaroche10] J. P. Delaroche *et al.* Phys. Rev. C **81**, 014303 (2010).

[Dewald89] A. Dewald *et al.* Zeitschrift fÃ¼r Physik A Hadrons and Nuclei **334**, 163 (1989).

[Dewald12] A. Dewald *et al.* Progress in Particle and Nuclear Physics **67**, 786 (2012).

[Dracoulis88] G. Dracoulis *et al.* Nuclear Physics A **486**, 414 (1988).

[Duchêne99] G. Duchêne *et al.* Nuclear Instruments and Methods in Physics Research Section A: Accelerators, Spectrometers, Detectors and Associated Equipment **432**, 90 (1999).

[Ekström08] A. Ekström *et al.* Phys. Rev. Lett. **101**, 012502 (2008).

[Ellegaard73] C. Ellegaard *et al.* Nuclear Physics A **206**, 83 (1973).

[Erler12] J. Erler *et al.* Nature **486**, 509 (2012).

[Gaffney13] L. Gaffney *et al.* Nature **497**, 199 (2013).

[Gascon87] J. Gascon *et al.* Nuclear Physics A **470**, 230 (1987).

[Goldring82] G. Goldring *et al.* Heavy Ion Collisions **3**, 484 (1982).

[Görgen10] A. Görgen. Journal of Physics G: Nuclear and Particle Physics **37**, 103101 (2010).

[Grahn08] T. Grahn *et al.* Nuclear Physics A **801**, 83 (2008).

[Grahn09] T. Grahn *et al.* Phys. Rev. C **80**, 014324 (2009).

[Guastalla13] G. Guastalla *et al.* Phys. Rev. Lett. **110**, 172501 (2013).

[Gueorguieva01] E. Gueorguieva *et al.* Nuclear Instruments and Methods in Physics Research Section A: Accelerators, Spectrometers, Detectors and Associated Equipment **474**, 132 (2001).

[Haxel49] O. Haxel *et al.* Phys. Rev. **75**, 1766 (1949).

[Heyde83] K. Heyde *et al.* Physics Reports **102**, 291 (1983).

[Heyde11] K. Heyde *et al.* Reviews of Modern Physics **83**, 1467 (2011).

[John14] P. R. John *et al.* Phys. Rev. C **90**, 021301 (2014).

[Joss01] D. Joss *et al.* Nuclear Physics A **689**, 631 (2001).

[Joss04] D. T. Joss *et al.* Phys. Rev. C **70**, 017302 (2004).

[Joss05] D. T. Joss *et al.* Journal of Physics G: Nuclear and Particle Physics **31**, S1715 (2005).

[Joss16] D. T. Joss *et al.* Phys. Rev. C **93**, 024307 (2016).

[Julin16] R. Julin *et al.* Journal of Physics G: Nuclear and Particle Physics **43**, 024004 (2016).

[Jungclaus11] A. Jungclaus *et al.* Physics Letters B **695**, 110 (2011).

[Kibédi08] T. Kibédi *et al.* Nuclear Instruments and Methods in Physics Research Section A: Accelerators, Spectrometers, Detectors and Associated Equipment **589**, 202 (2008).

[King00] S. L. King *et al.* Phys. Rev. C **62**, 067301 (2000).

[Krane88] K. S. Krane. Introductory nuclear physics. John Wiley & Sons (1988).

[Lazarus01] I. Lazarus *et al.* Nuclear Science, IEEE Transactions on **48**, 567 (2001).

[Le Blanc99] F. Le Blanc *et al.* Phys. Rev. C **60**, 054310 (1999).

[Lee88] J. K. P. Lee *et al.* Phys. Rev. C **38**, 2985 (1988).

[Lica16] R. Lica *et al.* Phys. Rev. C **93**, 044303 (2016).

[Luukko69] A. Luukko *et al.* Nuclear Physics A **135**, 49 (1969).

[Mayer48] M. G. Mayer. Phys. Rev. **74**, 235 (1948).

[Mccutchan15] E. Mccutchan. Nucl. Data Sheets **126**, 151 (2015).

[Milner71] W. Milner *et al.* Nuclear Physics A **177**, 1 (1971).

[Möller05] O. Möller *et al.* Phys. Rev. C **72**, 034306 (2005).

[Nilsson55] S. G. Nilsson *et al.* Kgl. Danske Videnskap. Selskab, Mat.-fys. Medd **29**, 1 (1955).

[Oganessian91] Y. T. Oganessian *et al.* Zeitschrift für Physik D Atoms, Molecules and Clusters **21**, S357 (1991).

[Pakarinen17] J. Pakarinen *et al.* Journal of Physics G: Nuclear and Particle Physics **44**, 064009 (2017).

[Paul95] E. S. Paul *et al.* Phys. Rev. C **51**, 78 (1995).

[Petkov92] P. Petkov *et al.* Nuclear Physics A **543**, 589 (1992).

[Petkov95] P. Petkov *et al.* Nuclear Physics A **589**, 341 (1995).

[Petkov01] P. Petkov *et al.* Nuclear Instruments and Methods in Physics Research Section A: Accelerators, Spectrometers, Detectors and Associated Equipment **457**, 527 (2001).

[Peura14] P. Peura. Spectroscopic studies of ^{173}Pt and ^{175}Pt. University of Jyvaskyla (2014).

[Podolyák09] Z. Podolyák *et al.* Phys. Rev. C **79**, 031305 (2009).

[Pritychenko16] B. Pritychenko *et al.* Atomic Data and Nuclear Data Tables **107**, 1 (2016).

[Radford95a] D. Radford. Nuclear Instruments and Methods in Physics Research Section A: Accelerators, Spectrometers, Detectors and Associated Equipment **361**, 306 (1995).

[Radford95b] D. Radford. Nuclear Instruments and Methods in Physics Research Section A: Accelerators, Spectrometers, Detectors and Associated Equipment **361**, 297 (1995).

[Rahkila08] P. Rahkila. Nuclear Instruments and Methods in Physics Research Section A: Accelerators, Spectrometers, Detectors and Associated Equipment **595**, 637 (2008).

[Ruotsalainen13] P. Ruotsalainen *et al.* Phys. Rev. C **88**, 024320 (2013).

[Saygi17] B. Saygi *et al.* Phys. Rev. C **96**, 021301 (2017).

[Singh02] B. Singh. Nucl. Data Sheets **95**, 387 (2002).

[Singh03] B. Singh. Nucl. Data Sheets **99**, 275 (2003).

[Singh15] B. Singh. Nucl. Data Sheets **130**, 21 (2015).

[Sorlin08] O. Sorlin *et al.* Progress in Particle and Nuclear Physics **61**, 602 (2008).

[Suhonen07] J. Suhonen. From Nucleons to Nucleus. Springer (2007).

[Talmi62] I. Talmi. Rev. Mod. Phys. **34**, 704 (1962).

[Taylor13] M. Taylor *et al.* Nuclear Instruments and Methods in Physics Research Section A: Accelerators, Spectrometers, Detectors and Associated Equipment **707**, 143 (2013).

[Tsunoda17] N. Tsunoda *et al.* Phys. Rev. C **95**, 021304 (2017).

[Virtanen95] A. Virtanen *et al.* Nuclear Physics A **591**, 145 (1995).

[Wood92] J. Wood *et al.* Physics Reports **215**, 101 (1992). doi:https://doi.org/10.1016/0370-1573(92)90095-H.